Mechanical Systems and Signal Processing 163 (2022) 108163

Contents lists available at ScienceDirect

Mechanical Systems and Signal Processing

journal homepage: www.elsevier.com/locate/ymssp

A quantitative assessment of the model form error of friction models across different interface representations for jointed structures

Justin H. Porter [a], Nidish Narayanaa Balaji [a], Clayton R. Little [b], Matthew R. W. Brake [a,*]

[a] *Department of Mechanical Engineering, Rice University, Houston, TX 77005, United States*
[b] *Department of Mechanical Engineering, Stanford University, Stanford, CA 94305, United States*

ARTICLE INFO

Communicated by John E Mottershead

Keywords:
Jointed Structures
Frictional systems
Hysteretic systems
Epistemic uncertainty
Optimization
Zero-thickness elements

ABSTRACT

Hysteretic models are widely used to model frictional interactions in joints to recreate experimental behavior. However, it is unclear which models are best suited for fitting or predicting the responses of structures. The present study evaluates 26 friction model/interface representation combinations to quantify the model form error. A Quasi-Static Modal Analysis approach (termed Rayleigh Quotient Nonlinear Modal Analysis) is adopted to calculate the nonlinear system response, and a Multi-Objective Optimization is solved to fit experimental data of the first mode of the Brake-Reuß Beam. Optimized parameters from the first mode are applied to the second and third bending modes to quantify the predictive ability of the models. Formulations for both tracing full hysteresis loops and recreating hysteresis loops from a single loading curve (Masing assumptions) are considered. Smoothly varying models applied to a five patch representation showed the highest flexibility (for fitting mode 1) and good predictive potential (for modes 2 and 3). For a second formulation, which uses 152 frictional elements to represent the interface, the physically motivated spring in series with a Coulomb slip model (elastic dry friction) has high error for fitting mode 1 and performs near the middle for predicting higher modes. For both interface representation, the best fit models are not the most physical, but rather the ones with the most parameters (as expected); however, the more physical models perform somewhat better for predicting the higher modes.

1. Introduction

Bolted joints are used throughout engineering applications, necessitating accurate models for design of systems. Arguably, the most popular modeling approach is representing frictional contact with hysteretic models (e.g., Iwan, Jenkins, or dry friction) to capture nonlinear softening and dissipation simultaneously [1,2]. Though many hysteretic models have been proposed for modeling friction in bolted joints [3], there is little consensus on the best modeling approaches to capture experimental behavior due to epistemic and aleatoric uncertainties (see Part V of [2]). Epistemic uncertainty is due to model form error since the exact physical mechanisms responsible for energy dissipation and transmission in jointed structures are not known. On the other hand, aleatoric uncertainty is

---

* Corresponding author.
E-mail addresses: jp88@rice.edu (J.H. Porter), nb25@rice.edu (N.N. Balaji), crl11@rice.edu (C.R. Little), brake@rice.edu (M.R.W. Brake).

https://doi.org/10.1016/j.ymssp.2021.108163
Received 9 September 2020; Received in revised form 27 May 2021; Accepted 18 June 2021

irreducible and comes from error in the estimates of the parameters for a given model.

Modeling approaches for joints can be divided into model fitting (or calibrated modeling) and predictive modeling. The first approach assumes a parametric model form whose parameters are adjusted based on experimental data [4–7]. These models can then be used to simulate the structure or predict the response of other similar structures [6]. In general, provided that a hysteretic model has a sufficiently large number of parameters, it is possible to calibrate it to a single or small number of excitation levels and modes; however, the limitations of this approach are that the physics are neglected and the model's utility and predictability outside of the calibration region is significantly limited.[1] This is thought to be due to the presence of epistemic error in the assumed model form. Popular models for calibration include the Jenkins model [8], the 4-parameter Iwan model [4], and a variety of other hysteretic models [3].

Though several studies have noted errors in model fits, few studies have attempted to compare multiple models. Of the comparison studies, many have used one numerical simulation as truth data. For instance, Oldfield et al. [9] compared parallel arrangements of a discrete number of parallel Jenkins elements (four to six) and a Bouc-Wen model to truth data of a high resolution model with Coulomb friction. They tuned the parallel Jenkins elements to match the hysteresis loop closely, but noted that the Bouc-Wen model was able to recreate the damping behavior but not the exact shape of the hysteresis loop. However, the practical utility of these comparisons is limited since other work has shown that high resolution models with Coulomb friction do not converge to the same behavior as experiments [2]. Other studies have been similarly limited to only a few models. For instance, some have compared parallel Jenkins elements to experiments [10], applied a least squares approach to fit a Bouc-Wen model to an Iwan model [11], fit Jenkins and 4- and 5-parameter Iwan models to experiments [6], and compared hysteresis loops of a single degree of freedom system with six different hysteretic models (Bouc-Wen, Jenkins, Iwan, Dahl, LuGre, Elasto-Plastic) [3].

One challenge for modeling jointed structures is the lack of friction models derived from the underlying physics of an interface. Recent models, such as the 5-parameter Iwan model [12], were proposed to give more flexiblity to fit experimental data that could not be adequately spanned by the 4-parameter Iwan model. Another recent model, the seven parameter friction model [13], was empirically derived to match the properties observed in lubricated contact. Even further, an eleven parameter Iwan model based on the seven parameter friction model was provided in [14] as an impractical demonstration of how an Iwan model can be generalized. Thus, a trend throughout the literature on hysteretic systems is the development of models with larger numbers of parameters. As previously noted, though, this comes at the cost of overfit models that are unable to be predictive outside of a narrow range.

The second area of active research is the development of predictive joint models. While predictive models have progressed, they are still not complete, requiring further models of both frictional interactions and kinematics of the joint. Studies have proposed using statistical distributions of asperities to predict friction forces under hysteretic loading without model fitting [15,16]. However, these studies were limited in the ability to reproduce experimental data with completely predictive models [15] or predict the friction coefficient for the model [16]. Other work has obtained reasonable estimates of friction coefficients using elastic–plastic asperity contact models with adhesion, but measurement limitations prevent practical application of the research [17]. Tribological approaches based on cellular automatons have also been used to build coupled physics models considering temperature, load, topography, friction, and wear to attempt to predict frictional behavior in a brake system [18–21]; however, the resulting models are developed for specific tribosystems and lack generalizability. The remaining challenges of building fully predictive models can be attributed to both aleatoric and epistemic uncertainties.

Experimental error further complicates the development of accurate joint modeling approaches [22]. Common assumptions about the relationship between bolt torque and bolt tension contain significant uncertainty [23]. Some recent work has sought to reduce this uncertainty by measuring bolt strain values [16], or to infer preload by measuring the natural frequencies of the bolts themselves [24]. Another common assumption in modeling is that the surfaces are completely flat, which is not perfectly realized in experimental setups. Calibrated models fit experimental data including the experimental error resulting in parameters that do not perfectly represent the desired physics. These model parameters, therefore, have additional error due to the original experimental error limiting their applicability to other structures.

This study seeks to quantify the epistemic uncertainty of friction models to identify the best models and model features. This is accomplished through multi-objective optimization (MOO) to fit simulations to experimental modal frequency and damping. This captures both of the primary phenomena of interest for joints, softening and dissipation, resulting in a set of solutions (a Pareto front) since the two objectives may not be optimized by the same parameters. The epistemic uncertainty is then quantified by calculating the area between the Pareto front and a shared lower bound. This procedure of calibrated modeling reduces the aleatoric uncertainty by allowing the parameters of the system to vary and minimize the error in the model fit. However, given enough parameters, the procedure can overfit the data, so this does not guarantee that the models with the lowest error describe the actual physics the best. Rather, the models with the lowest errors are the most flexible allowing them to fit the experimental data the best. Additional assessments of the model form error are conducted by considering the parameters optimized for the first bending mode applied to the second and third bending modes. This study makes use of the vibration and bolt strain data from [16] to reduce experimental uncertainty.

The rest of the paper is organized into five sections. First, the full details of the friction models are presented (Section 2). Next, in Section 3 the physical system and modeling procedure are introduced. These sections are followed by the results (Section 4) for the whole-joint (five patch formulation) simulations and the full-joint (reduced 152-element formulation) simulations. Lastly, the

---

[1] Calibrated modeling overfits the experimental data and generally cannot be done for multiple modes.

Table 1
Overview of friction models and number of parameters. The Bouc-Wen $n = 1$ model has 3 or 4 parameters for the Masing and non-Masing cases respectively.

Microslip Models (Number of Parameters)		Bilinear Models (Number of Parameters)	
4-Parameter Iwan	(5)	Jenkins	(3)
5-Parameter Iwan	(6)	Elastic Dry Friction	(3)
General Bouc-Wen	(4)	Prager	(3)
Bouc-Wen $n = 1$	(3 or 4)	Generalized Jenkins Prager	(4)
Bouc-Wen $n = 2$	(3)		
Valanis	(5)		

conclusions are summarized in Section 5.

2. Contact models

The present study considers 26 friction model and interface representation combinations referenced to experimental data on a single bolted structure, assessed within a consistent quasi-static framework. The considered models are divided between four bilinear friction models and six microslip models. The simple bilinear friction models have been developed for use with high resolution meshes (hundreds or thousands of Degrees of Freedom (DOFs)) to capture joint behavior with relatively few parameters. The simplest model is the Jenkins model consisting of an initial linear spring and then a constant slip force [8]. Related to the Jenkins model, the second model included in this study is an elastic dry friction model that has an initial stiffness and a slip force dependent on the normal contact force [25]. The Prager model, consisting of a slip force and a post-slip stiffness [26], is also considered. The final bilinear friction model is the Generalized Jenkins Prager model, which is a combination of the Jenkins and Prager models.

The considered microslip models are commonly used to model joints with a few (tens of) contact DOFs since they provide smooth force–displacement relationships with fewer DOFs. The present study considers the 4- [4] and 5-parameter Iwan models [12], both of which are derived from a distribution of Jenkins elements and are commonly used in the joints community. The rate form Bouc-Wen model, along with two special cases of the Bouc-Wen model that have analytical solutions, is also considered (see [27] for a review of uses of the Bouc-Wen model). The Valanis model considered in this paper is a rate form hysteretic model that includes a post-slip stiffness that has recently come into use in the joints community [5,28]. Lastly, the present study considers supplementing a number of the microslip models with a post-slip stiffness that has previously been added to some models [29,30]. For broader reviews of hysteretic models and their applications to joints, the interested reader is referred to [31,32,3].

An overview of the considered friction models is presented in Table 1. The friction models are applied to two reduced order models: the whole-joint reduced order model (WJROM) with tens of DOFs and the full-joint reduced order model (FJROM) with hundreds of DOFs (see Section 3.2). The ten models in Table 1, plus additional models created by adding a post-slip stiffness, are considered for the Masing WJROM (12 models), the non-Masing WJROM (5 models), the WJROM without viscous damping (4 models), and the non-Masing FJROM (5 models), resulting in the 26 considered interface representations. The microslip and bilinear friction models are considered with the WJROM, but only the bilinear friction models are considered with the FJROM due to the computational cost.

Many of the WJROM models are considered in both a Masing and a non-Masing framework (see Section 2.3.1). The force–displacement relationships for the Masing models are reduced to consider only monotonic loading while the non-Masing relationships allow for hysteretic reversal points. All of the FJROM models are implemented into the non-Masing framework. The WJROM and FJROM models also differ in that the WJROM decouples tangential force–displacement relationships while the FJROM simulations use tangentially coupled, directionally invariant traction-displacement relationships. Due to the limitations of the quasi-static framework (see Section 3.4), no explicit velocity dependence is considered in any of the friction models.

The WJROM and FJROM also differ in that the WJROM is formulated to use force–displacement relationships while the FJROM is formulated to use traction-displacement relationships. However, parameters for the WJROM models are scaled, as necessary, by the associated moment(s) of area for each DOF such that the frictional forces for a given displacement, applied to multiple DOFs, are proportional to the associated areas of each DOF. Further details about the model reduction and the implications of force versus traction relationships are discussed in Section 3.2.

The rest of this section first describes the normal contact models that are shared between many of the friction models (Section 2.1). Then, the details of all of the tangential friction models are provided (Section 2.2). The section concludes with modeling considerations for the friction models (Section 2.3). Except when noted otherwise, parameters for the different friction models are allowed to take on any positive value.

2.1. Normal contact models

Most models use a normal contact spring unless otherwise noted. For a normal stiffness k_n and a normal displacement u_n, the normal force f_n is

$$f_n = k_n u_n \tag{1}$$

for the WJROM simulations. For the FJROM, the normal traction t_n given a normal stiffness per unit area of k_n is

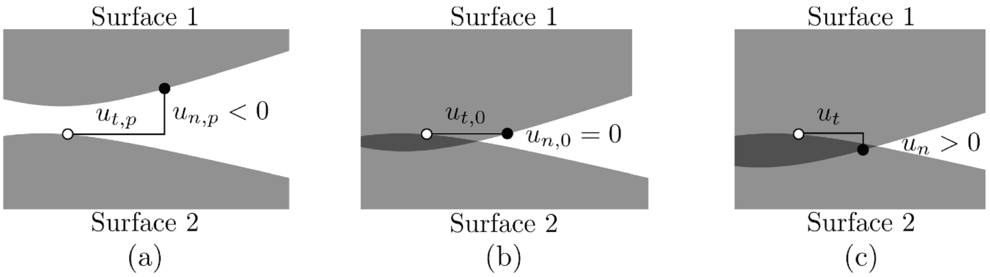

Fig. 1. Schematic representations of reestablishing contact: (a) initially separated configuration (previous instant), (b) interpolated point of reestablished contact, and (c) configuration at the current instant.

$$t_n = k_n u_n \tag{2}$$

and is integrated to get normal forces on the DOFs.

The second normal contact model is the penalty contact, which is used for the elastic dry friction simulations and Generalized Jenkins Prager with penalty contact simulations. In these cases, the normal force for the WJROM simulations is

$$f_n = \begin{cases} k_n u_n & u_n > 0 \quad (contact) \\ 0 & u_n \leqslant 0 \quad (separation) \end{cases} \tag{3}$$

and the normal traction for the FJROM simulations is

$$t_n = \begin{cases} k_n u_n & u_n > 0 \quad (contact) \\ 0 & u_n \leqslant 0 \quad (separation) \end{cases} \tag{4}$$

When the interface is separated, all tangential forces or tractions are set to zero if the penalty normal contact model is used. For both normal contact models, the parameter k_n is fit alongside the tangential friction model parameters.

When non-Masing hysteresis loops are generated, information about the state of the system when the displacement changes direction (i.e., the reversal point) is necessary. If contact is maintained throughout the simulation, this is the displacement and force or traction at the reversal point. However, if the interface separates with a penalty contact model, the reversal point must be set when contact is reestablished. In these cases, the tangential displacement for the reversal point is estimated via linear interpolation between normal displacements as

$$u_{t,0} = \frac{0 - u_{n,p}}{u_n - u_{n,p}} \left(u_t - u_{t,p} \right) + u_{t,p}. \tag{5}$$

Here, $u_{t,0}$ is considered as the point where contact is reestablished (see Fig. 1), and the subscript p indicates the displacements at the previous instant. The force or traction at the reversal point is then set to zero.

2.2. Friction models

The 10 tangential friction models that are presented in Table 1 are described herein. The elastic dry friction model is dependent upon the normal contact model; whereas the other models, such as the 4-Parameter Iwan model, are independent of the normal contact forces or tractions.

2.2.1. The 4-Parameter Iwan model

The 4-parameter Iwan model [4,32,33] was derived as a summation of an infinite number of frictional sliders with tangential stiffnesses and different slip forces. A distribution for the Iwan element for joints was proposed as

$$\rho(\phi) = R\phi^{\chi}[H(\phi) - H(\phi - \phi_{max})] + S\delta(\phi - \phi_{max}), \tag{6}$$

where $H(\cdot)$is the Heaviside function, $\delta(\cdot)$ is the Dirac-delta function, ϕ represents the displacement that causes slip of a specific slider in the distribution, ϕ_{max} is the upper bound of ϕ, χ controls the exponent of dissipation, R controls the microslip force, and S allows for a slope discontinuity of the force–displacement relationship at the beginning of macroslip. This equation can be integrated and converted to more physical parameters of f_s (macroslip force), k_t (tangential stiffness), and β (ratio of microslip to macroslip stiffness) [4]. The resulting force–displacement relationship for monotonic loading is

$$f(u) = \begin{cases} k_t u - \left(\left(\dfrac{k_t \left(\beta + \frac{\chi+1}{\chi+2} \right)}{f_s(1+\beta)} \right)^{1+\chi} \dfrac{k_t}{(1+\beta)(\chi+2)} \right) u^{\chi+2} & u < \phi_{max} \\ f_s & u \geqslant \phi_{max} \end{cases}, \tag{7}$$

with the displacement for macroslip

$$\phi_{max} = \frac{f_s(1+\beta)}{k_t \left(\beta + \frac{\chi+1}{\chi+2} \right)}. \tag{8}$$

From experimental observations, [4] recommends the parameter $\chi \in (-1,0]$. Thus, for the 4-parameter Iwan model, the parameters to be fit are f_s, k_t, χ, and β.

2.2.2. The 5-Parameter Iwan model

A 5-parameter Iwan model [12] was developed as an extension of the 4-parameter Iwan model [4] to reduce the slip force at macroslip, similar to a stiction model that has a separate static and dynamic coefficient of friction. The ratio of slip force to force required to initiate slip is the fifth parameter $\theta \in [0, 1]$, with the case of $\theta = 1$ being the 4-parameter Iwan model. The force–displacement relationship for monotonic loading becomes

$$f(u) = \begin{cases} k_t u + \left(\left(\dfrac{k_t \left(\beta + \frac{\chi+1}{\chi+2} \right)}{f_s(1+\beta)} \right)^{1+\chi} \dfrac{k_t(\chi+1)}{(1+\beta)} \right) \left(\dfrac{\theta}{\chi+2} - \dfrac{1}{\chi+1} \right) u^{\chi+2} & u < \phi_{max} \\ \theta f_s & u \geqslant \phi_{max} \end{cases} \tag{9}$$

with the value of ϕ_{max} calculated with (8). Like the 4-parameter Iwan model, the variables to be fit for the 5-parameter Iwan model are f_s, k_t, χ, β, and θ.

2.2.3. The general Bouc-Wen model

The Bouc model was proposed for modeling hysteretic behavior [34] and then extended to the Bouc-Wen model in [35]. The differential equation for the Bouc-Wen model for a displacement u and traction t can be written to be independent of time as

$$\frac{dt}{du} = A - [\alpha \operatorname{sgn}(t\dot{u}) - \beta] |t|^n. \tag{10}$$

Here, A is an initial stiffness and α, β, and n govern the shape of the hysteresis loop. The operator $\operatorname{sgn}(\cdot)$ is the signum function that returns the sign of the argument. The handling of the rate-form Bouc-Wen model within the quasi-static framework is discussed further in Section 2.3.2. When the Masing assumptions are applied, only initial loading from the origin is considered, so the differential equation simplifies to

$$\frac{dt}{du} = A - \eta |t|^n \tag{11}$$

in terms of η, which is used as a single parameter in place of α and β. Based on thermodynamic analysis, it has been shown that parameters must be chosen such that $\alpha \geqslant 0, \beta \in [-\alpha, \alpha]$, and $n > 0$ [36]. The conditions on α and β result in $\eta \geqslant 0$. The Bouc-Wen model is applied only to the WJROM, but, unlike other models, is formulated in terms of tractions t. For a variable n, there is no constant (parameter independent) way to scale the parameters A and η such that the force due to a give displacement is always proportional to the patch area. The force f at a given displacement is calculated by multiplying the traction t by the patch area.

Though the original Bouc-Wen model [35] includes a hysteretic force (represented by (10)) and a conservative stiffness, this paper uses the Bouc-Wen model to refer to only the hysteretic model without an additional stiffness unless otherwise noted. Consequently, the parameters to be fit for the Masing general Bouc-Wen model are A, η, and n.

2.2.4. The Bouc-Wen $n = 1$ Model

An analytical solution to (10) can be obtained for the case of $n = 1$ and $\alpha \neq \pm\beta$. The full solution is [3]

$$f = \begin{cases} -\dfrac{A}{(\alpha-\beta)}\left(c_1 e^{-(\alpha-\beta)u} - 1\right)(\dot{u} > 0) \cap (f > 0) \\ \dfrac{A}{(\alpha+\beta)}\left(c_2 e^{(\alpha+\beta)u} - 1\right)(\dot{u} < 0) \cap (f > 0) \\ \dfrac{A}{(\alpha-\beta)}\left(c_3 e^{(\alpha-\beta)u} - 1\right)(\dot{u} < 0) \cap (f < 0) \\ -\dfrac{A}{(\alpha+\beta)}\left(c_4 e^{-(\alpha+\beta)u} - 1\right)(\dot{u} > 0) \cap (f < 0) \end{cases}, \tag{12}$$

where the c_i's are constants calculated based on continuity of the force–displacement relationship at reversal or transition points.

For the Masing case, only monotonic loading from the origin is considered; therefore, the friction model can be further reduced to

$$f = \begin{cases} -\dfrac{A}{\eta}\left(e^{-\eta u} - 1\right)(\dot{u} > 0) \cap (f > 0) \\ \\ \dfrac{A}{\eta}\left(e^{\eta u} - 1\right)(\dot{u} < 0) \cap (f < 0) \end{cases} \tag{13}$$

by combining the parameters for α and β into a single parameter η. Therefore, the parameters A and η need to be fit for the Masing case, or A, α, and β for the non-Masing case.

2.2.5. The Bouc-Wen $n = 2$ model

An analytical solution to (10) can also be obtained for the case of $n = 2$ and $\alpha \neq \pm\beta$ as [3]

$$f = \begin{cases} \sqrt{\dfrac{A}{\alpha-\beta}}\tanh\left(u\sqrt{A(\alpha-\beta)} + c_1\right) f\dot{u} > 0 \\ \\ \sqrt{\dfrac{A}{\alpha+\beta}}\tan\left(u\sqrt{A(\alpha+\beta)} + c_2\right) f\dot{u} < 0 \end{cases} \tag{14}$$

with constants c_i calculated from the reversal points. Since the Bouc-Wen $n = 2$ model is only considered for Masing cases, only forward loading is considered reducing the force–displacement relationship to

$$f = \sqrt{\frac{A}{\eta}}\tanh\left(u\sqrt{A\eta}\right) \tag{15}$$

in terms of a single parameter η that is used instead of the two parameters α and β. Similarly to the Masing $n = 1$ case, the parameters to be fit for the Masing $n = 2$ case are A and η.

2.2.6. The Valanis model

The Valanis model was originally proposed as an endochronic plasticity model consistent with thermodynamics based on an intrinsic time measure [37], and then later applied to bolted connections [38] as

$$\frac{df}{du} = E_0\left(\frac{1 + \mathrm{sgn}\left(\dot{u}\right)\frac{\lambda}{E_0}(E_t u - f)}{1 + \kappa\,\mathrm{sgn}\left(\dot{u}\right)\frac{\lambda}{E_0}(E_t u - f)}\right). \tag{16}$$

Here, E_0 and E_t are the stiffnesses in the initial and slipped regimes. The system can be varied from a linear spring to a stick–slip element by varying κ from 0 to 1, and the force at the onset of slip, σ_0, can be varied with λ [38] as

$$\sigma_0 = \frac{E_0}{\lambda\left(1 - \kappa\frac{E_t}{E_0}\right)}. \tag{17}$$

The handling of the rate-form Valanis model within the quasi-static framework is discussed further in Section 2.3.2. The parameters to be fit for the Valanis model are thus E_0, E_t, λ, and κ.

2.2.7. The Jenkins model

The simplest bilinear friction model is the Jenkins model [8], constructed as a spring in series with a Coulomb friction element. In terms of the tangential stiffness k_t and the slip force f_s, the tangential force–displacement relationship for monotonic loading of the WJROM is

$$f_t = \begin{cases} k_t u_t & |k_t u_t| < f_s \\ f_s \operatorname{sgn}(u_t) & Otherwise \end{cases} \tag{18}$$

For hysteretic loading of the WJROM, the force–displacement relationship for decoupled x and y directions is

$$f_t = \begin{cases} \underbrace{k_t(u_t - u_{t,0}) + f_{t,0}}_{f_{t,stuck}} & |f_{t,stuck}| < f_s \\ f_s \operatorname{sgn}(u_t - u_{t,0}) & Otherwise \end{cases} \tag{19}$$

defined in terms of the displacement and force at the reversal point, $u_{t,0}$ and $f_{t,0}$ respectively. For the FJROM model, the directionally invariant traction-displacement relationship for direction q (either x or y), slip traction t_s, and loading reversal point $u^q_{t,0}$ and $t^q_{t,0}$ is

$$t^q_t = \begin{cases} \underbrace{k_t(u^q_t - u^q_{t,0}) + t^q_{t,0}}_{t^q_{stuck}} & \sqrt{{t^x_{stuck}}^2 + {t^y_{stuck}}^2} < t_s \\ t_s \dfrac{t^q_{stuck}}{\sqrt{{t^x_{stuck}}^2 + {t^y_{stuck}}^2}} & Otherwise \end{cases} \tag{20}$$

Hence, for this implementation of the Jenkins model, f_s and k_t for the WJROM or t_s and k_t for the FJROM are the parameters that need to be fit.

2.2.8. The elastic dry friction model

The elastic dry friction model has a tangential stiffness like the Jenkins model, but uses a slip force that is dependent on the normal force or traction [25]. Therefore, the elastic dry friction model uses the same equations as the Jenkins model with two changes. First, the normal penalty contact model (all forces or tractions are zero when surfaces are separated) is used instead of the normal spring model. Second, instead of a parameter for f_s or t_s, a parameter is chosen for the coefficient of friction (μ). The slip force or traction is then the normal force or traction times the coefficient of friction ($f_s = \mu f_n$ or $t_s = \mu t_n$). Consequently, the two tangential parameters for the elastic dry friction model are μ and k_t.

2.2.9. The Prager model

The Prager model has a set valued force less than the slip force at zero displacement and a linear spring added to the slip force at nonzero displacements [26]. The Prager model in one dimension for a tangential force f_t can be expressed in terms of the slip force f_s and the post-slip stiffness k_p by

$$\begin{cases} f_t \in [-f_s, f_s] & u_t = 0 \\ f_t = f_s \operatorname{sgn}(u_t) + k_p u_t & u_t \neq 0 \end{cases} \tag{21}$$

This set valued relationship is not compatible with the quasi-static framework used in this paper, so it is regularized with a linear stiffness k_t through the origin. This results in the Generalized Jenkins Prager model (Section 2.2.10). However, the tangential stiffness k_t is fixed as a constant, so that the Prager model does not return the same results as the Generalized Jenkins Prager model. In addition, the value of k_t is chosen to be larger than any other model fitting values of k_t to ensure that it acts as a penalty stiffness rather than influencing the dynamics. This leaves the two tangential parameters to be fit as f_s and k_p.

2.2.10. The Generalized Jenkins Prager model

The Generalized Jenkins Prager model is the combination of the Jenkins model (see Section 2.2.7) with a post-slip stiffness. The monotonic loading force–displacement relationship for both tangential directions of the WJROM is

$$f_t = \begin{cases} k_t u_t + k_p u_t & |k_t u_t| < f_s \\ f_s \operatorname{sgn}(u_t) + k_p u_t & Otherwise \end{cases} \tag{22}$$

For the FJROM model, the stuck prediction of the Jenkins traction for direction q (either x or y) is

$$t^q_{stuck} = k_t\left(u^q_t - u^q_{t,0}\right) + t^q_{t,0} \tag{23}$$

for a loading reversal point of $u^q_{t,0}$ and $t^q_{t,0}$. For a slip traction t_s, the slip traction in direction q is

$$t^q_{slip} = t_s \frac{t^q_{stuck}}{\sqrt{{t^x_{stuck}}^2 + {t^y_{stuck}}^2}} \tag{24}$$

Then, the directionally invariant traction-displacement relationship is

$$t^q_t = \begin{cases} t^q_{stuck} + k_p\left(u_t - u_{t,0,k_p}\right) & \sqrt{{t^x_{stuck}}^2 + {t^y_{stuck}}^2} < t_s \\ t^q_{slip} + k_p\left(u_t - u_{t,0,k_p}\right) & Otherwise \end{cases} \tag{25}$$

The reversal traction is calculated solely based on the Jenkins contributions to the traction as

$$t^q_{t,0} = \begin{cases} t^q_{stuck} & \sqrt{{t^x_{stuck}}^2 + {t^y_{stuck}}^2} < t_s \\ t^q_{slip} & Otherwise \end{cases} \tag{26}$$

The quantity $u_{t,0,k_p}$ for the FJROM traction relationships is the reference point for the post-slip stiffness spring. This quantity is only nonzero for the FJROM Generalized Jenkins Prager with penalty contact model when the interface separates and then reestablishes contact, in which case it is set to $u_{t,0}$ as calculated by (5). The model fitting parameters are f_s, k_t, and k_p for the WJROM or t_s, k_t, and k_p for the FJROM.

2.3. Modeling considerations

The following subsections discuss the application of the Masing hypotheses to the considered friction models, the application of the rate form friction models, and the addition of a post-slip stiffness to a general friction model.

2.3.1. Masing assumptions

The Masing hypotheses are commonly applied to bolted joints to calculate dissipation. The Masing hypotheses state [4,2]:

- That a full hysteresis loop can be recreated from the initial loading curve by scaling the displacement and force by a factor of two, reflecting it across both axes, and translating it to match reversal points.
- The force–displacement relationship is dependent on the previous reversal point, and if the hysteretic curve crosses a previous curve, then it must follow the previous curve.

The application of these hypotheses allows for dissipation to be calculated solely from the initial forward loading of the system, reducing computational costs. The Masing hypotheses can be applied to either the modal acceleration of the full system or the local dissipation of the friction law (see Section 3.4).

Though many of the models are considered within a Masing framework, not all of the considered models follow the Masing hypotheses. For loading starting from the origin, the Jenkins, Prager, Generalized Jenkins Prager, and Iwan models all obey the Masing hypotheses at the local level. The models that use penalty contact do not locally obey the Masing hypotheses because the tangential force–displacement or traction-displacement relationships are coupled to the normal forces or tractions. Lastly, by comparing initial loading and hysteretic unloading slopes, it can be shown that the Bouc-Wen models and the Valanis model do not locally obey the Masing hypotheses except for in the linear cases.

2.3.2. Rate form models

The general Bouc-Wen model (see Section 2.2.3) and the Valanis model (see Section 2.2.6) are both rate form models and thus require numerical integration. The models provide an equation that describes the rate of change of the force f with respect to displacement u for a parameter set $\underset{\sim}{X}$ or

$$g\left(u, f, \underset{\sim}{X}\right) = \frac{df}{du}. \tag{27}$$

This equation is then integrated with a mixed 4th/5th order Runge–Kutta method (the Dormand-Prince algorithm [39]). For the Masing simulations, the initial conditions of the integration are zero force and displacement. For the non-Masing simulations, the initial conditions are the force and displacement at the previous reversal point.

In addition, the parameter derivatives of the final force are desired for the optimization (see Section 3.5.1). Extending the method

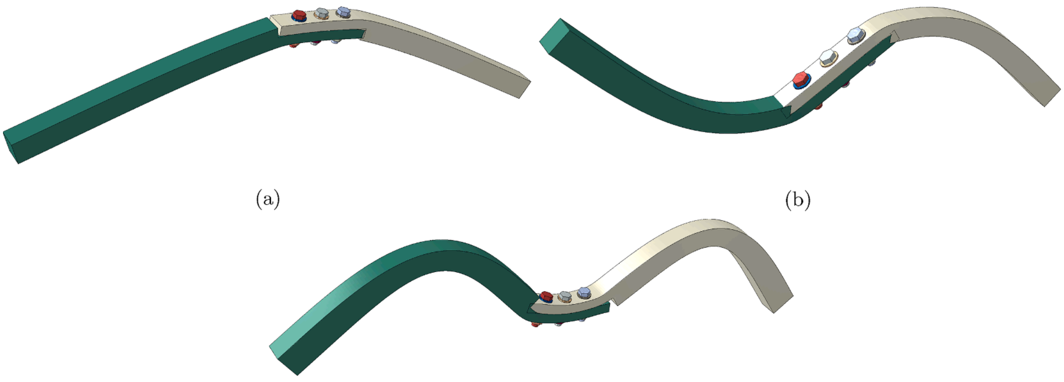
(a) (b)

(c)

Fig. 2. Deformed shapes of (a) first bending mode, (b) second bending mode, and (c) third bending mode (linearized about a static prestress simulation).

for obtaining derivatives for the shooting method [40], the parameter derivatives are calculated using the property that

$$\frac{d}{du}\left[\frac{\partial f\left(u,\underset{\sim}{X}\right)}{\partial C}\right]=\frac{\partial}{\partial C}\left[g\left(u,f\left(u,\underset{\sim}{X}\right),\underset{\sim}{X}\right)\right]=\frac{\partial g\left(u,f\left(u,\underset{\sim}{X}\right),\underset{\sim}{X}\right)}{\partial f\left(u,\underset{\sim}{X}\right)}\left[\frac{\partial f\left(u,\underset{\sim}{X}\right)}{\partial C}\right]+\frac{\partial g\left(u,f,\underset{\sim}{X}\right)}{\partial C} \tag{28}$$

for function g from (27) and a chosen parameter $C \in \underset{\sim}{X}$. This equation can then be numerically integrated for every parameter along with (27). The initial conditions for the parameter derivatives are zero for initial loading or the values at the previous reversal point for loading with hysteretic reversal points.

For dissipation calculations (see Section 3.4), the area A_D under the force–displacement relationship and associated derivatives are also calculated via numerical integration. The derivative of A_D with respect to the displacement is the current force. The parameter derivatives are calculated by integrating the expression

$$\frac{d}{du}\left[\frac{\partial A_D\left(u,\underset{\sim}{X}\right)}{\partial C}\right]=\frac{\partial f\left(u,\underset{\sim}{X}\right)}{\partial C}. \tag{29}$$

2.3.3. Post-slip stiffness

Similarly to how the Generalized Jenkins Prager model (see Section 2.2.10) is the Jenkins model (see Section 2.2.7) with an additional post-slip stiffness, the post-slip stiffness k_p is added to several other models.[2] This is accomplished through adding a constant linear stiffness, which also increases the initial stiffness (e.g., the initial stiffnesses of the Jenkins and Generalized Jenkins Prager models are k_t and $k_t + k_p$ respectively). The addition of the post-slip stiffness adds the parameter k_p to the set of parameters to be optimized for a given model. For a model denoted X, the associated model with post-slip stiffness is

---

[2] This modeling decision was made following observations that existing models with a post-slip stiffness (e.g., the Valanis model) performed extremely well during the initial portions of the study; see Section 4.7.

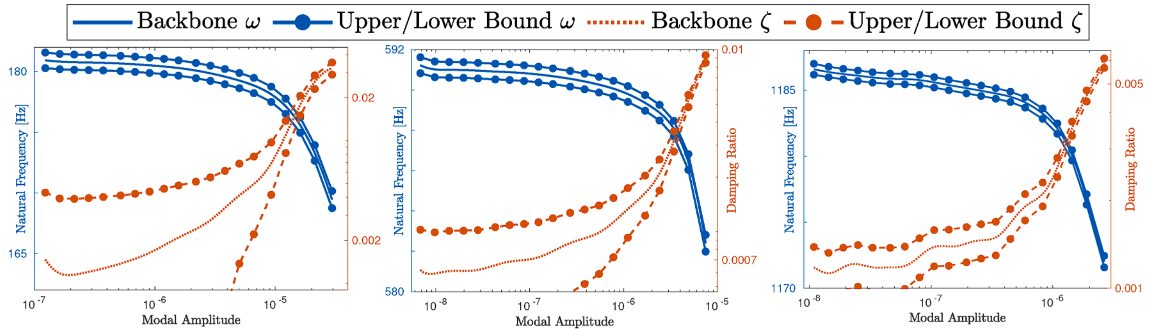

(a) (b) (c)

Fig. 3. Experimental frequency and damping response of the (a) first bending mode, (b) second bending mode, and (c) third bending mode. The upper and lower bounds are equal distances from the backbone on a linear scale. The plot limits of the damping are set such that the behavior of the backbone can seen and thus cut off the plot of the lower bound.

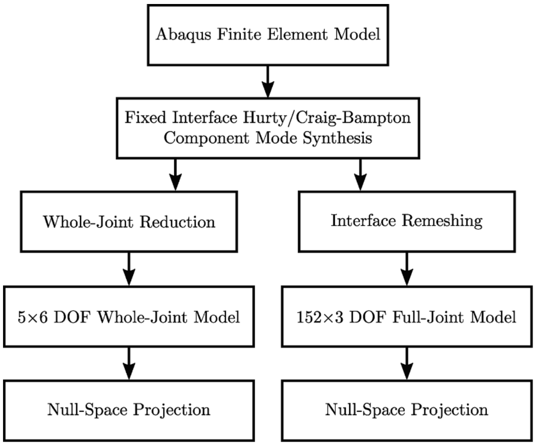

Fig. 4. Overview of model reduction procedure.

$$f_{X+k_p*u} = f_X + k_p\left(u_t - u_{t,0,k_p}\right), \tag{30}$$

where $u_{t,0,kp}$ is the reference point of the post-slip stiffness spring. When the normal spring contact model is used (i.e., (1) or (2)), $u_{t,0,k_p}$ is always zero, and when the normal penalty contact model is used (i.e., (3) or (4)), $u_{t,0,k_p}$ starts as zero. If the interface separates and reestablishes contact, then $u_{t,0,kp}$ is set to $u_{t,0}$ using (5). As with the Generalized Jenkins Prager model, reversal point forces or tractions used for calculations after a reversal are taken only from the underlying model (i.e., Jenkins for the Generalized Jenkins Prager case or X for the general case).

For all models, the contributions of the post-slip stiffness are added to the two directions separately. Since the post-slip stiffness is a linear spring, the directionally invariant FJROM friction models with coupled x and y directions remain directionally invariant after adding the post-slip stiffness contributions to both the x and y tractions.

3. System model

3.1. System of Interest (BRB)

The present study considers the three-bolt lap joint in the Brake-Reuß Beam (BRB). The first three bending modes of the system (linearized about a static prestress simulation) are presented in Fig. 2. The experimental data is taken from [16], and the experimental setup is briefly summarized here. Engineering drawings of the system can be found in [6].

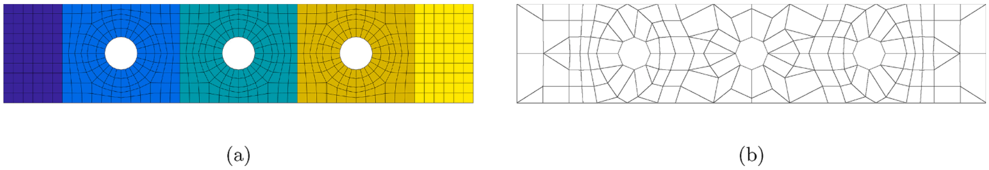

Fig. 5. Interface representations: (a) original mesh from Abaqus colored for WJROM patches and (b) FJROM remeshed interface.

For testing, the BRB was assembled with strain gauge instrumented bolts that measured a prestress force of 12.845 kN per bolt.[3] The system was then suspended with two bungee cables to mimic free-free boundary conditions. Acceleration is recorded with an accelerometer on the end of the beam for seven impact hammer tests.

The ring-down acceleration data was filtered with a 4th-order Butterworth bandpass filter and then processed with the Peak-Finding and Fitting (PFF) method [41]. This process gives the amplitude dependent modal frequency and damping for the mode of interest that is then used for model fitting. The amplitude of the experimental data is scaled by the magnitude of the response node in the numerical mass normalized mode shape from a linear eigenvalue analysis of the prestressed state. This scaling is done for an initial set of parameters for each model and not repeated during the model fitting procedure.

The experimental procedure resulted in very repeatable backbone curves for the system. A Gaussian Process Regression [42] is used to process the raw amplitude-frequency and amplitude-damping data points generated by the PFF algorithm into a smooth backbone (see Fig. 3). This process also generates upper and lower bounds that contain approximately 95% of the amplitude-frequency or amplitude-damping data points. In addition, the amplitude range of the experimental data is larger than previous model fitting efforts with a frequency shift of 11.5 Hz for the first mode compared to about 2–5 Hz [7,43].

3.2. Model reduction framework

The present study uses a reduced representation of the system with fewer linear and non-linear Degrees of Freedom (DOFs). Specifically, a hyper-reduction method is used that allows for the nonlinear forces to be calculated using the reduced DOFs without an intermediary transformation to the original DOFs. The full details of the model reduction technique are described in [44] and briefly summarized here. Because the reduction reduces the number of linear and nonlinear DOFs, it results in a model that has a significantly lower computational cost than either the full order model or a standard reduced order model (e.g., such as one formed by substructuring with Hurty/Craig-Bampton models).

For both models, first an Abaqus finite element model is created of the structure with free-free boundary conditions. This model is reduced to the interface degrees of freedom (588 × 3) plus 19 fixed interface modes using the Fixed Interface Hurty/Craig Bampton Component Mode Synthesis method [45,46]. The whole-joint reduction and interface remeshing procedures are then applied to obtain the WJROM and FJROM respectively [44]. Fig. 4 shows an overview of the model reduction procedure, and Fig. 5 shows the initial interface mesh, patches for the whole-joint reduced order model (WJROM), and the remeshed interface for the full-joint reduced order model (FJROM). After the model reduction, the six fully-fixed rigid body modes are constrained out via a null-space projection, but the zero energy mode of the interface separating along the bolt-axis is preserved to allow for the nontrivial contributions of relative motion to the system response [16]. The prestress analysis (see Section 3.3), conducted with a contact model, eliminates this zero energy mode.

The WJROM has five “non-stiffening” patches[4] with three translational and three rotational DOFs. Frictional models relate the six DOFs of a patch to forces and moments applied to the same patch. The WJROM has a total of 43 DOFs corresponding to the 30 patch DOFs plus 13 fixed interface modes left from the Hurty/Craig Bampton reduction (after the 6 fully-fixed rigid body modes are removed). Since the WJROM has only a few DOFs, it cannot fully capture the kinematics of the interface. Therefore, microslip friction models (e.g., Iwan or Bouc-Wen; see Section 2.2) typically are applied to the interface. However, the current study also applies simpler models (e.g., Jenkins) for comparison.

The FJROM has 152 Zero-Thickness Elements (ZTEs) with three translational DOFs at each node. The use of ZTEs assumes that there are small displacements on the interface such that the same set of nodes on the two interfaces remain in contact. This significantly reduces computational cost by eliminating contact searches. The ZTEs of the remeshed interface for the FJROM are chosen based on the PD-objective remeshing[5] and show converged results to the underlying mesh (588 × 3 DOFs) for the elastic dry friction model in [44]. The reduced mesh DOFs are connected to the original mesh via a Galerkin projection, i.e., the Lagrange shape functions of the reduced mesh on the original mesh will be represented exactly in an L2 sense. The tractions on the remeshed interface are calculated based on the remeshed DOFs without requiring any calculations on the original mesh, due to the formulation employed (see [44] for the exact details). The FJROM has 505 DOFs including the 456 DOFs associated with the translational DOFs of each ZTE. The

---

[3] This prestress resulted from a bolt torque of, approximately, 20 Nm. The exact value varied from bolt to bolt and test to test, which is why the prestress was controlled for instead.

[4] The patch DOFs represent the original DOFs without being rigidly connected such that the stiffness of the system is not modified [44].

[5] The objective is the normalized sum of the normal pressure from the a prestress analysis and mass-weighted modal displacements of the first mode [44].

additional DOFs come from preserving more fixed interface modes during a Hurty/Craig Bampton reduction in the interface remeshing procedure. For each ZTE, the frictional relationship is evaluated to calculate tractions from displacements. An integration matrix, created in the model reduction procedure, is used to integrate the tractions into forces applied at the DOFs. Since the FJROM has sufficient DOFs to capture the kinematics of the interface, simpler friction models with fewer parameters are generally employed (e.g., Jenkins).

Though the WJROM and FJROM are formulated to use force–displacement and traction-displacement relationships, respectively, contact models act consistently between the two reductions since the WJROM uses parameters that are scaled between DOFs such that forces at a given displacement are proportional to the patch area. The formulation of the WJROM uses forces since the use of tractions implies a constant traction across the patch, which generally is not true, especially for constitutive models accounting for the rotational DOFs of the patch. On the other hand, the FJROM is formulated based on the assumption that tractions can be evaluated at the quadrature points. Though the WJROM formulation allows for constitutive models that account for rotational angles of the patches, none of the considered models use the rotational DOFs or calculate moments produced at the patches because such equations are not generally available for the considered friction models.

For both reduced systems, a relative coordinate system between the two sides of the interface is used. The coordinate systems are setup such that positive displacements input into the friction models result in positive internal forces or tractions (see Section 2.2). In addition, negative displacements normal to the interface correspond to separation of the two surfaces (see Section 2.1). For a system with N DOFs, this leads to the governing nonlinear dynamics equations of motion

$$\mathbf{M}\underset{\sim}{\ddot{x}} + \mathbf{K}\underset{\sim}{x} + \underset{\sim}{f_{nl}} = \underset{\sim}{f} + \underset{\sim}{f_s}. \tag{31}$$

Here, $\underset{\sim}{x}$ is the $N \times 1$ displacement vector; $\mathbf{M}$ and $\mathbf{K}$ are the $N \times N$ mass and stiffness matrices respectively; $\underset{\sim}{f_{nl}}$, $\underset{\sim}{f_s}$, and $\underset{\sim}{f}$ are nonlinear (frictional), static (prestress), and external forces respectively ($N \times 1$ vectors).

3.3. Prestress solution

Previous work has shown that including a prestress analysis is critical for matching modal frequencies in model fitting, reducing the frequency error by two orders of magnitude in [6]. To this end, all simulations start with a prestress analysis using the experimentally measured bolt tensions. The prestress calculation is carried out on the WJROM and FJROM using a vector generated in the model reduction procedure to distribute forces appropriately. The prestressed solution is calculated with a gradient-based nonlinear root finding algorithm (the trust-region dogleg method implemented in MATLAB's `fsolve` routine [47]). The frictional force–displacement (for the WJROM) or traction-displacement (for the FJROM) relationships are generally used in the prestress analysis. During the optimization procedure, the prestress calculations are updated for each set of friction parameters. This differs from other studies using quasi-static methods, which typically use linear springs during the prestress phase, and in doing so neglect some frictional and contact effects [48].

In this study, two different frictional formulations are used: those that satisfy the Masing assumptions (see Section 2.3.1), and those that violate the Masing assumptions. The application of these modeling choices results in two different approaches for incorporating the prestress into the simulations. For the Masing simulations (restricted to the WJROMs), the force and displacement from the prestress simulations are used in the nonlinear force evaluation as

$$\underset{\sim}{f_{nl}}\left(\underset{\sim}{u}\right) = \underset{\sim}{f_{nl}}\left(\underset{\sim}{u} - \underset{\sim}{u_s}\right) + \underset{\sim}{f_{nl}}\left(\underset{\sim}{u_s}\right) \tag{32}$$

in which $\underset{\sim}{u_s}$ and $\underset{\sim}{f_{nl}}\left(\underset{\sim}{u_s}\right)$ are the displacement and force from the prestress analysis. For the non-Masing models (which span a portion of the WJROM and all of the FJROM simulations), the prestress displacement and force or traction are used as initial reversal point information in the friction models (quantities denoted with a subscript 0 in Section 2).

Lastly, for some non-Masing WJROM simulations (see Section 4.2), the prestress analysis is conducted without including the hysteretic portion of the frictional forces and is referred to as a conservative prestress analysis. The conservative prestress analysis does include the linear normal contact stiffness and the linear effects of the post-slip stiffness. This modeling decision is made because the models show frictional shakedown behavior[6] [49]. In addition, for a single DOF system, the conservative prestress analysis with the considered quasi-static framework is most consistent with reference frequency domain simulations [50] for such cases.

3.4. Nonlinear modal analysis

Nonlinear modal analysis is conducted using a Quasi-Static Modal Analysis (QSMA) method termed Rayleigh Quotient-based Nonlinear Modal Analysis (RQNMA) [51]. The recent popularity of QSMA methods stems from the implicit condensation method

---

[6] Under repeated oscillations, frictional forces evolve to oscillate around a different mean force than the initial prestressed force if the prestress analysis includes nonconservative forces for some models.

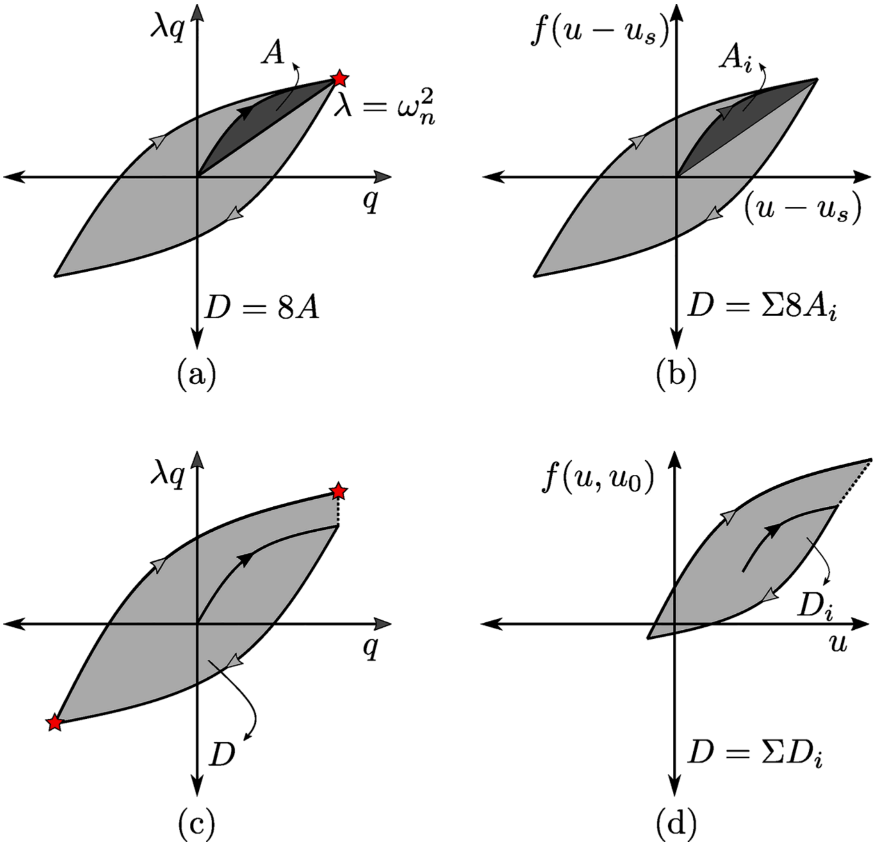

Fig. 6. Schematic representations of dissipation for (a) Masing modal level hysteresis, (b) Masing local hysteresis, (c) non-Masing modal level hysteresis, and (d) non-Masing local hysteresis. Black arrows represent initial loading, grey arrows represent hysteretic unloading and reloading. The stars mark points where the Rayleigh quotient is used to calculate modal frequency. In (d), the initial loading starts offset from the origin due to prestress displacements and forces.

[52] that was further developed into current QSMA methods [53,54,43]. QSMA methods are advantageous mainly due to the computational simplicity in comparison to other (frequency or time domain) approaches.[7] RQNMA solves for the response of the structure with coupled static and dynamic forces, which is necessary for interfacial models in which preload forces can change with time. This differs from other work that considers the dynamical nonlinear problem as a perturbation about the prestressed state [43,55], and are thus limited to Masing models and other simplifications of the interfacial relationships (see [43] for instance, which simplifies the preload as invariant). The computational advantage of RQNMA makes the parametric investigations of the present paper feasible. Previous work has used QSMA approaches to model experimental data [6,43], and RQNMA has been verified against previous QSMA and frequency domain methods [51].

RQNMA [51] results in solving the equations

$$\mathbf{K}\underset{\sim}{u}+\underset{\sim}{f_{nl}}-\lambda\mathbf{M}\left(\underset{\sim}{u}-\underset{\sim}{u_s}\right)-\underset{\sim}{f_s}=0 \tag{33a}$$

$$\left(\underset{\sim}{u}-\underset{\sim}{u_s}\right)^T\mathbf{M}\left(\underset{\sim}{u}-\underset{\sim}{u_s}\right)-q^2=0 \tag{33b}$$

at a desired scalar modal amplitude q to determine amplitude dependent modal characteristics. In these equations, $\underset{\sim}{u}$ and $\underset{\sim}{u_s}$ are the current and static displacements, respectively, and λ is a scalar Lagrange multiplier corresponding to the modal amplitude constraint equation (interpreted as the square of the natural frequency through analogy to linear systems). Since (33) is solved numerically, there are nonzero residuals in the evaluation of the left hand side of the system of equations. Cases where the nonlinear solver fails to converge to the RQNMA solution, resulting in high residuals, are discussed further in Sections 3.5.2 and 4. Unlike other formulations of

---

[7] See [51] for a discussion of merits of RQNMA compared to other methods.

QSMA that use a modal amplitude based on a modal filter, RQNMA uses a mass normalization constraint (33b) to define the modal amplitude. The amplitude dependent natural frequency and mode shape can be extracted as

$$\omega_n(q) = \sqrt{\lambda(q)} \tag{34a}$$

$$\phi\left(q\right) = \frac{1}{q}\left(\underset{\sim}{u} - \underset{\sim}{u_s}\right) \tag{34b}$$

respectively. For the non-Masing simulations, the natural frequency is averaged between the values calculated at $\pm q$.

Dissipation is calculated within the RQNMA framework by considering the area of a hysteresis loop constructed by varying the modal amplitude from $+q$ to $-q$ and then back to $+q$ (see Fig. 6 for the four different ways considered in this paper). Modal level dissipation is the area in the plot of modal acceleration λq as a function of modal amplitude q. The current study uses Legendre-Gauss-Lobatto quadrature of variable order to integrate the modal hysteresis loops. Alternatively, for some WJROM simulations, dissipation is determined locally by integrating the force–displacement relationships. Because of the reduction in computational cost, the local analytical calculation of dissipation is preferred, but is not possible for the WJROM elastic dry friction model due to the penalty contact or the FJROM simulations due to the coupling of the tangential directions [55]. The Masing Assumptions discussed in Section 2.3.1 are also applied for a set of the WJROM simulations to calculate dissipation from just the forward hysteretic loading.

For non-Masing simulations, the hysteresis loop constructed with RQNMA need not return to the same point as the initial loading. In these cases, the hysteresis loop is traced multiple times to converge the damping calculation and any remaining gap is closed with a single line. The Masing simulations are not affected by hysteresis loops not closing due to the formulation of the Masing assumptions to only use the initial loading curve.

In previous QSMA approaches, the modal acceleration is derived via a modal filter [54,43]

$$\phi^T\left(\boldsymbol{K}\underset{\sim}{u} + \underset{\sim}{f_{nl}}\right) = \phi^T[\boldsymbol{M}\phi(\lambda q)] = \lambda q. \tag{35}$$

However, this method of derivation is not consistent with RQNMA, in which the mode shapes are amplitude dependent. Instead of requiring that the force be parallel with the mode shape, the virtual work associated with the generalized coordinate set as the modal amplitude q is considered. Rearranging (33a) by placing all physical forces on the left side and taking the discrete inner product with the virtual displacement yields

$$\left[\frac{\partial \underset{\sim}{u}}{\partial q}\delta q\right]^T\left[\boldsymbol{K}\underset{\sim}{u} + \underset{\sim}{f_{nl}} - \underset{\sim}{f_s}\right] = \left[\frac{\partial \underset{\sim}{u}}{\partial q}\delta q\right]^T \lambda \boldsymbol{M}\left(\underset{\sim}{u} - \underset{\sim}{u_s}\right) \tag{36}$$

for the virtual work. To simplify the right hand side, the derivative of (33b) with respect to q gives

$$\left[\frac{\partial \underset{\sim}{u}}{\partial q}\right]^T \boldsymbol{M}\left(\underset{\sim}{u} - \underset{\sim}{u_s}\right) = q \tag{37}$$

since $\boldsymbol{M}$ is symmetric. Substituting this into (Eq. 36) yields

$$\left[\frac{\partial \underset{\sim}{u}}{\partial q}\delta q\right]^T\left[\boldsymbol{K}\underset{\sim}{u} + \underset{\sim}{f_{nl}} - \underset{\sim}{f_s}\right] = \left[\frac{\partial \underset{\sim}{u}}{\partial q}\delta q\right]^T \lambda \boldsymbol{M}\left(\underset{\sim}{u} - \underset{\sim}{u_s}\right) = \lambda q \delta q. \tag{38}$$

By analogy to Lagrangian mechanics, the virtual work associated with displacement $\delta q$is $\lambda q \delta q$, and λq is the corresponding generalized force termed the "modal acceleration." In the linear case, this reduces to previous derivations based on the modal filter since the displacements evolve along the mode shape or $\frac{\partial \underset{\sim}{u}}{\partial q} = \phi$.

The dissipation, $D(q)$, is converted to an effective viscous damping factor, $\zeta(q)$, by analogy to linear systems [56]

$$\zeta\left(q\right) = \frac{D(q)}{2\pi(\omega_n(q)q)^2}. \tag{39}$$

Except for the results presented in Section 4.3, the lowest amplitude damping, $\zeta_{0,exp}$, from the experimental data set is added to $\zeta(q)$ as

$$\zeta\left(q\right) = \frac{D(q)}{2\pi(\omega_n(q)q)^2} + \zeta_{0,exp} \tag{40}$$

to act as viscous modal damping independent of amplitude.

3.5. Multi-objective optimization

The present study solves a multi-objective optimization (MOO) problem [57] to fit both the modal frequency and damping of the first mode of the Brake-Reuß beam resulting in a Pareto front or non-dominated set, which can be used to interpret model form error (see Section 3.7). Reinterpreting dominances for the error minimization of model fitting, a solution $\underset{\sim}{X}^{(1)}$ dominates a different solution $\underset{\sim}{X}^{(2)}$ when [57]:

1. The solution $\underset{\sim}{X}^{(1)}$does not have greater error in any objective than $\underset{\sim}{X}^{(2)}$or $f_j(\underset{\sim}{X}^{(1)})\leqslant f_j(\underset{\sim}{X}^{(2)})$for all $j = 1, 2, \ldots, M$.
2. The solution $\underset{\sim}{X}^{(1)}$has strictly lower error in at least one objective than $\underset{\sim}{X}^{(2)}$or $f_j(\underset{\sim}{X}^{(1)}) < f_j(\underset{\sim}{X}^{(2)})$for at least one $j \in \{1, 2, \ldots, M\}$.

Using this definition of dominance, the non-dominated set is defined as the subset of solutions that are not dominated by any other solution in the original set [57]. A non-dominated set of the entire search space is called a Pareto-optimal set or a Pareto front [57].

In this study, a combination of a boundary intersection method [58] and a genetic algorithm [57] is used to fit numerical simulations to experimental data to produce Pareto fronts. The optimization problem in terms of the parameter set $\underset{\sim}{X}$ in the domain of valid parameters Ω for N amplitude levels is

$$\min_{\underset{\sim}{X}\in\Omega}\begin{pmatrix} f_\omega\left(\underset{\sim}{X}\right) \\ f_\zeta\left(\underset{\sim}{X}\right)\end{pmatrix} = \begin{pmatrix} \sqrt{\dfrac{1}{N}\displaystyle\sum_{i=1}^{N}\left(\dfrac{\Delta\omega\left(q_i;\underset{\sim}{X}\right)}{\omega(q_i)}\right)^2} \\ \sqrt{\dfrac{1}{N}\displaystyle\sum_{i=1}^{N}\left(\dfrac{\Delta\ln\zeta\left(q_i;\underset{\sim}{X}\right)}{\ln\zeta(q_i)}\right)^2}\end{pmatrix}. \tag{41}$$

Though all plots use these error metrics, the actual optimization is considered on log-scale with the mean-squared error as

$$\min_{\underset{\sim}{X}\in\Omega}\begin{pmatrix} \log_{10}\left(f_\omega\left(\underset{\sim}{X}\right)^2\right) \\ \log_{10}\left(f_\zeta\left(\underset{\sim}{X}\right)^2\right)\end{pmatrix} = \begin{pmatrix} \log_{10}\left(\dfrac{1}{N}\displaystyle\sum_{i=1}^{N}\left(\dfrac{\Delta\omega\left(q_i;\underset{\sim}{X}\right)}{\omega(q_i)}\right)^2\right) \\ \log_{10}\left(\dfrac{1}{N}\displaystyle\sum_{i=1}^{N}\left(\dfrac{\Delta\ln\zeta\left(q_i;\underset{\sim}{X}\right)}{\ln\zeta(q_i)}\right)^2\right)\end{pmatrix}. \tag{42}$$

Since the relationship between these error metrics is monotonic, the minimum in one should be equivalent to the minimum in the other. However, the log-scale error metrics do not change by orders of magnitude, improving numerical conditioning. Throughout the discussion of the results (see Section 4), the term model fitting errors or just errors refers to the values $f_\omega\left(\underset{\sim}{X}\right)$ and $f_\zeta\left(\underset{\sim}{X}\right)$ from (41) unless otherwise noted.

The error metric of (41) is similar to that of previous model fitting efforts, but uses the error in natural frequency rather than the error in the frequency shift [7,43]. The present study compares the total frequency so that the model fitting effort matches both the low amplitude frequency and the shifts in frequency unlike previous studies that permitted significant deviations in the low amplitude frequency [7].

3.5.1. Boundary intersection

Where possible, a boundary intersection method [58] is used to solve the MOO problem. Boundary intersection is a constrained optimization problem to find a local minimum. First scalar optimizations in terms of modal frequency and damping are conducted yielding error values of $f_\omega^*\left(\underset{\sim}{X}\right)$ and $f_\zeta^*\left(\underset{\sim}{X}\right)$ respectively. These two values taken together represent the utopian point, or the best possible error in both metrics. For some models, the scalar optimization produces poor results, so the utopian point is estimated from an initial genetic algorithm optimization. Given the utopian point, a constrained optimization is conducted along a vector at an angle ψ originating from the utopian point. Mathematically, the optimization problem can be expressed as

$$\begin{gathered}\min t \\ s.t.\left(\begin{matrix} log_{10}\left(f_\omega\left(\underset{\sim}{X}\right)^2\right) log_{10}\left(f_\zeta\left(\underset{\sim}{X}\right)^2\right)\end{matrix}\right) - \left(\begin{matrix} log_{10}\left(f_\omega^*\left(\underset{\sim}{X}\right)^2\right) log_{10}\left(f_\zeta^*\left(\underset{\sim}{X}\right)^2\right)\end{matrix}\right) = t\begin{pmatrix} cos\psi \\ sin\psi\end{pmatrix}.\end{gathered} \tag{43}$$

Table 2

Experimental frequency and damping variabilities using the optimization error metric (41) for upper and lower bounds in Fig. 3. The damping variabilities for the lower bound are higher because of the logarithmic handling of damping factor with (41). The lower bound variability for mode 1 is not defined since some amplitudes have negative values.

	Upper Bound Variabilities		Lower Bound Variabilities	
	Frequency	Damping	Frequency	Damping
Mode 1	3.55e−03	1.29e−01	3.55e−03	NaN
Mode 2	6.62e−04	5.34e−02	6.62e−04	1.02e−01
Mode 3	3.36e−04	1.89e−02	3.36e−04	2.20e−02

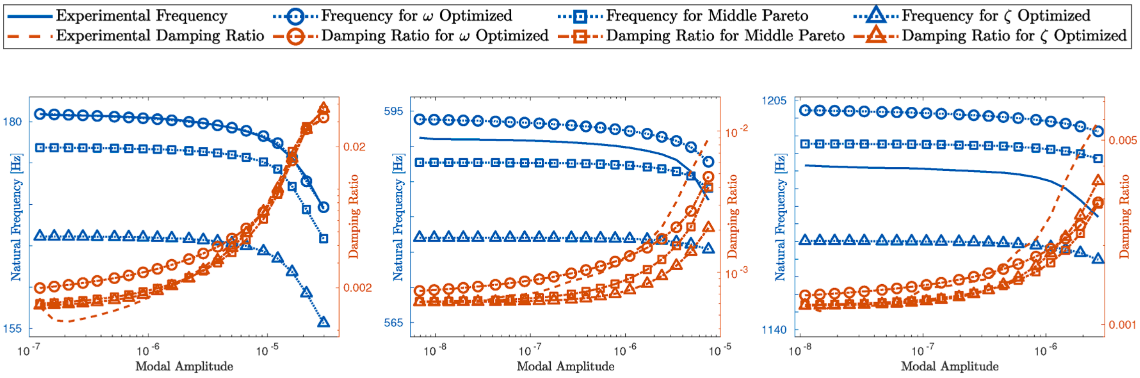

(a) (b) (c)

Fig. 7. Example backbone plots for the WJROM Masing 4-parameter Iwan model (a) first, (b) second, and (c) third bending modes.

Table 3

Errors for 4-parameter Iwan model fits plotted in Fig. 7 using (41).

	Frequency Optimized Errors		Middle Parameter Set Errors		Damping Optimized Errors	
	Frequency	Damping	Frequency	Damping	Frequency	Damping
Mode 1	8.78e−04	5.57e−02	2.03e−02	2.80e−02	7.97e−02	2.24e−02
Mode 2	4.76e−03	4.94e−02	4.77e−03	6.91e−02	2.21e−02	1.10e−01
Mode 3	1.42e−02	4.86e−02	7.16e−03	5.46e−02	1.66e−02	4.29e−02

MATLAB’s `fmincon` function is used for the numerical implementation of the constrained optimization problem [59–61]. The Pareto front is swept out by solving the optimization problem multiple times with different angles $\psi \in \left[0, \frac{\pi}{2}\right]$. A non-dominated sorting is applied to the final results from the optimization to eliminate any points not on the Pareto front.

Boundary intersection is the preferred optimization method since it is deterministic and the solution can be checked to verify that it is a local minimum. However, there is not a guarantee that the local minimum that is found is the global minimum. Additionally, boundary intersection requires implementing gradients with respect to parameter values in the error calculation. As a practical note, the present implementation of boundary intersection only works for the Masing WJROM simulations; however it does not provide satisfactory performance for all of the models, and is discussed further in Section 4.1.

3.5.2. Genetic algorithm

Where the current implementation of the boundary intersection method fails to converge, MATLAB’s `gamultiobj` function (a variant of the NSGA-II algorithm [57]), with generations of 100 members for the WJROMs or 75 members for the FJROMs, is used to produce Pareto fronts. Unlike purely elitist algorithms, which always maintain the best population members, the variant of the NSGA-II algorithm balances diversity and model fitting error to improve convergence and search the entire population space. However, this means that Pareto optimal solutions from one generation can be eliminated during the transition to the next generation. To capture all of the available information about the Pareto front, the results from the last 50 generations are combined for the non-dominated sorting. For all genetic algorithm optimizations (see Section 4), the default convergence criteria is used to end all simulations (the spread remains within a tolerance of 1e-4 for 100 generations). In addition, the distance crowding measure is set to “genotype” for all genetic algorithm optimizations so that the algorithm maintains diversity in the parameter space.

For initial tests of the genetic algorithm with some models, some parameter sets resulted in frequency or damping errors that dominated large sections of the Pareto front, but had very high residuals for the nonlinear RQNMA solution (see Section 3.4). Slight

Table 4
Lower and upper bound reference points for area calculation.

	Frequency		Damping	
	Lower	Upper	Lower	Upper
Mode 1	7.12e−04	1.70e−01	1.98e−02	5.00e−01
Mode 2	6.62e−04	1.70e−01	2.20e−02	5.00e−01
Mode 3	3.36e−04	1.70e−01	1.89e−02	5.00e−01

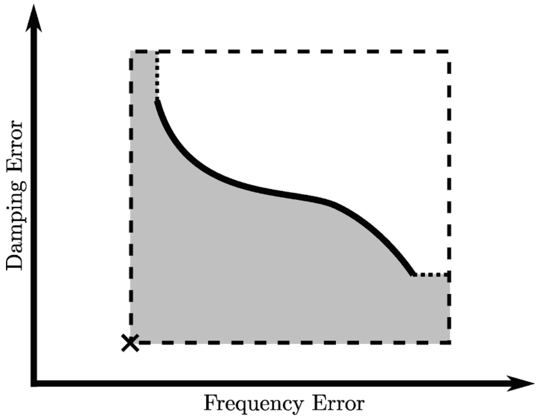

Fig. 8. Schematic representations of area calculation. The solid black curve is the calculated Pareto front and is extended by the dotted lines to the edge of the box. The dashed box is the considered bounding box given in Table 4 and the x is the lower corner of the box (included in the plots in Section 4). The area of the shaded region with axes on linear scales is calculated to quantify the uncertainty.

perturbations to these sets of parameters would result in significantly different model fitting errors. To prevent the genetic algorithm from preserving these non-converged points, the L1 norms of the residuals for the RQNMA solutions are added to the final errors for the optimization of some models. For Masing simulations, the norm of the residual at each frequency evaluation is added. For non-Masing simulations, the residuals from the final two $+q$ evaluations and the final $-q$ at each amplitude are added to the final errors for the optimization. Since the model fitting errors are calculated on a log-scale (see (42)), the residuals of converged RQNMA solutions are much smaller in magnitude than the calculated model fitting errors and thus do not affect the selection of converged simulations by the genetic algorithm. However, for the non-converged simulations, the norm of the RQNMA residuals approaches the magnitude of the log-scale model fitting errors and thus significantly increases the likelihood of the solution being eliminated by the genetic algorithm. The parameter sets found through the optimization are rerun through the model fitting error calculation to obtain the error values plotted throughout this paper without the inclusion of the norm of the RQNMA residuals.

3.6. Contextualization of error

To contextualize the errors produced from model fitting, the optimization error metric (41) is applied to the upper and lower experimental bounds of Fig. 3 yielding the numerical values in Table 2. Recent experimental benchmarks for frequency variability of impact testing yielded ranges of 0.13%, 0.070%, 0.086% for the first three modes respectively [22]. The experimental data used here has around three times the variability for mode 1, but lower variabilities for modes 2 and 3.

Table 2 gives an assessment of the variability of the experiments that can be directly compared to the error in model fits. If a model fit can achieve errors that are less than the experimental variability, it cannot be concluded whether the error is due to model form error or variations in the experiment. On the other hand, if the model fitting errors are higher than the experimental variability, then model form error must be contributing to the error in the fit. Therefore these variabilities provide an estimate of the desired model fitting errors.

To visualize the errors associated with a typical model, three of the optimized backbones are plotted for the 4-parameter Iwan model in Fig. 7. For comparison to the experimental variabilities, Table 3 tabulates the errors for the plotted backbones. Here, all of the mode 1 fits achieve damping errors less than experimental variability. The frequency optimized backbone also achieves frequency errors less than experimental variability for mode 1 and damping errors less than experimental variability for mode 2. This suggests that the mode 1 errors can be attributed to experimental variability while the mode 2 and 3 errors represent a combination of experimental variability, overfitting to mode 1, and model form error.

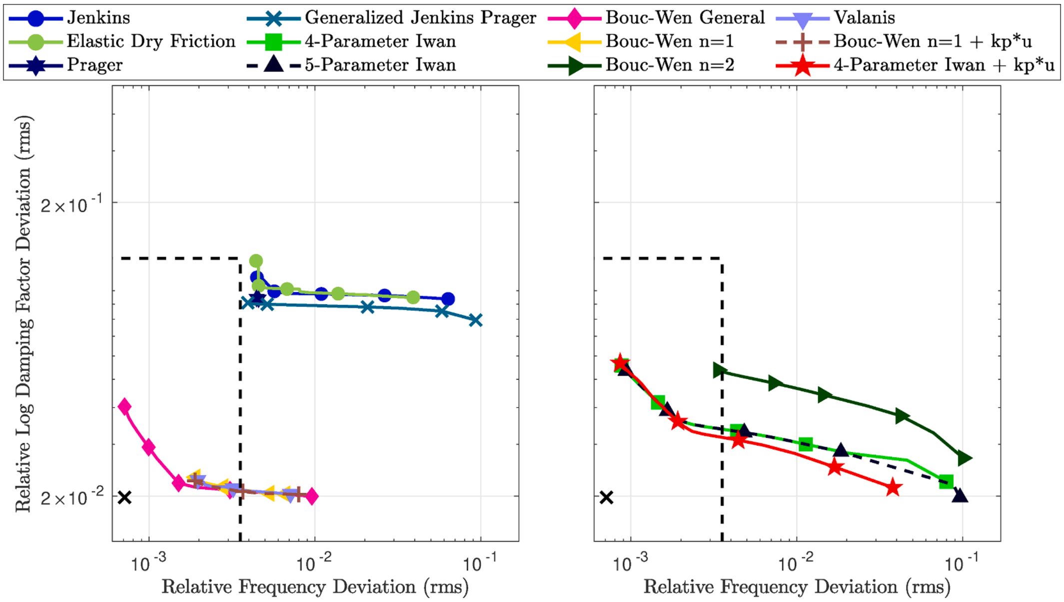

Fig. 9. Masing WJROM Pareto fronts for mode 1 with shared y-axes. The dashed box represents experimental variability and the black x is the reference point for calculating the quantitative measure of epistemic uncertainty. The data is plotted in separate figures for clarity.

3.7. *Epistemic uncertainty*

The epistemic uncertainty is compared between models graphically and quantitatively. Graphically, model fitting error values closer to the origin indicate that the models produce better fits. The Pareto fronts for the first mode are produced through the model fitting procedure (see Section 3.5) and then plotted. The parameters from the model fit for the first mode are then applied to model the second and third modes to calculate errors. For the first mode, lower errors are interpreted as the model being more flexible. For the second and third modes, lower errors indicate that model parameters translate better between modes and therefore that the model may be more representative of the actual physics.

The uncertainty is quantified by the area between the non-dominated set of solutions and a lower bound of the minimum between all model fits for the given mode and the experimental variability (see Table 4). For the first mode, the non-dominated set is the plotted Pareto front. For the second and third modes, the errors are calculated using the parameters from the mode 1 fitting and are not restricted to a single non-dominated set. The non-dominated set using solely the second mode and then solely the third mode errors is determined and used in the area calculation for the second and third modes respectively.

Since none of the non-dominated sets reach zero error in either error metric, the quantitative uncertainty measure is calculated by the fraction of the region that the non-dominated sets does not dominate. The upper bounds of the region are taken as the upper bounds of the Pareto front plots and are provided in Table 4. The process is shown schematically in Fig. 8 where the ends of the Pareto front are extended to an outer box and then the area of the shaded region is calculated. The integration is carried out using the trapezoid rule. Additionally, since the end points of the Pareto front are not necessarily the utopian points for the model, the quantitative estimate of the epistemic uncertainty is not exact. Rather, it provides a metric for comparing which groups of models behave similarly.

4. Results

Using the system model described in Section 3 and the friction models from Section 2, this section assesses the epistemic uncertainty by determining the Pareto fronts for each model. First the WJROM is used within a Masing framework (Section 4.1) then a non-Masing framework (Section 4.2). The WJROM is also considered without viscous damping contributions in Section 4.3. Then the FJROM model is considered within the non-Masing framework (Section 4.4). A quantitative comparison of all considered modeling approaches is presented in Section 4.5, and a comparison of simulation times is presented in Section 4.6. For each set of results, first the Pareto fronts for the first mode are presented with analysis. Then, the Pareto optimal parameters from the first mode are applied to calculate errors of the second and third bending modes. All optimizations consider twenty amplitude levels, logarithmically spaced, for comparison between the experimental data and numerical simulations. For all of the model fits, ranges of the Pareto optimal parameter sets are presented in Section A for reference. Finally, model fits are provided for a different version of the experimental backbones in Section 4.7 to show the sensitivity to the experimental data.

Table 5
Backbone plots for different WJROM Masing models.

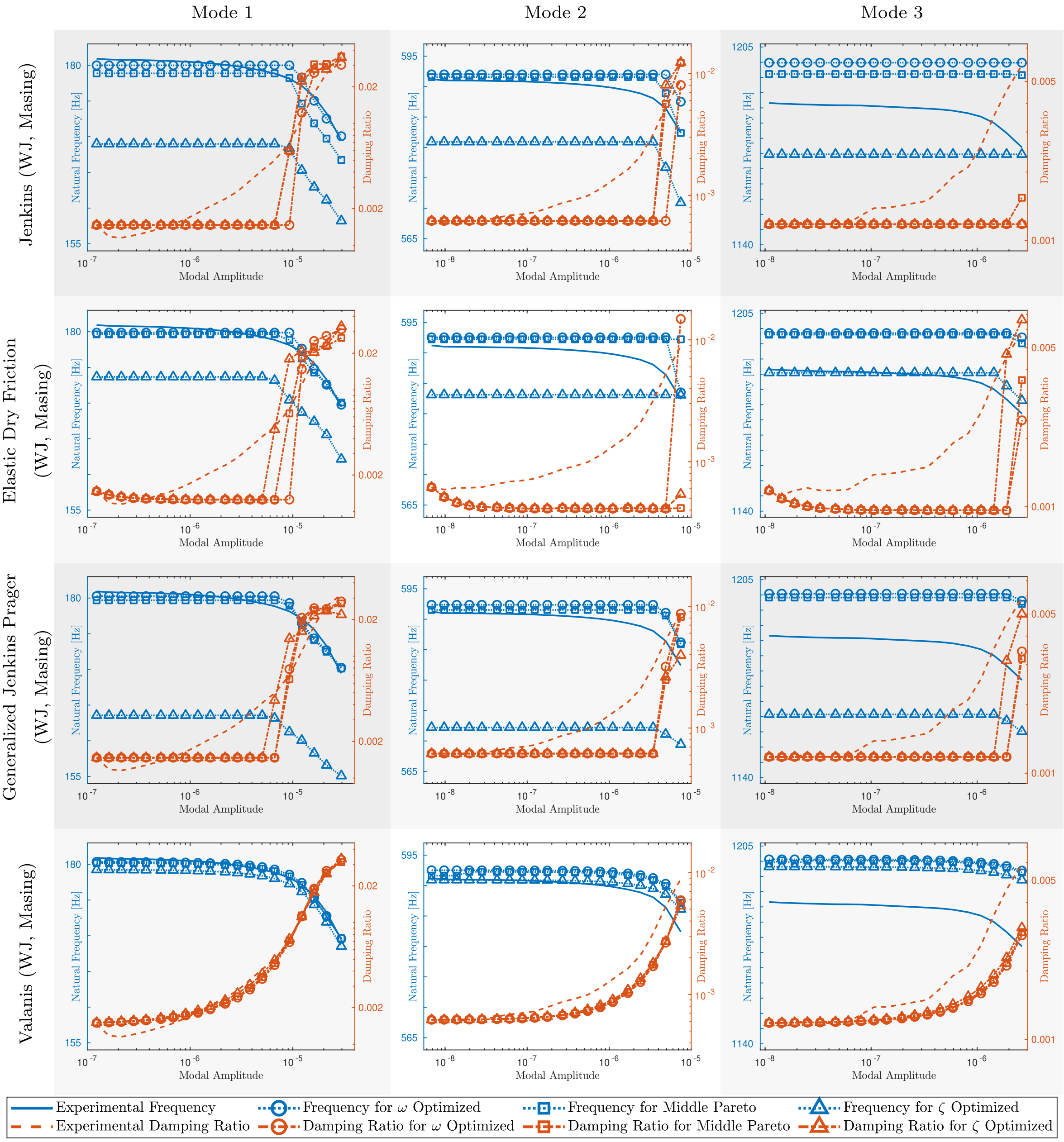

4.1. WJROM Masing

4.1.1. Mode 1

The first set of model fits are produced for the WJROM using the Masing assumptions and, therefore, are based solely on the response to monotonic loading (see Section 2.3.1). Fig. 9 shows the Pareto fronts for the first bending mode for each model.

The boundary intersection method is used for most of the optimizations, but the current implementation did not produce satisfactory results for the elastic dry friction or Prager models, which instead use the genetic algorithm (see Section 3.5 and the end of this section for a comparison of the methods). Initial fits for elastic dry friction with the genetic algorithm produced high residuals for the nonlinear RQNMA solution suggesting that the solutions were not valid, so the residual penalization scheme (see Section 3.5.2) was

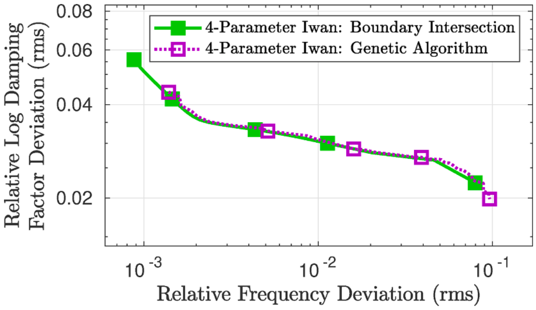

Fig. 10. Comparison of Masing WJROM Pareto fronts for mode 1 for the 4-parameter Iwan model obtained with the boundary intersection method and the genetic algorithm.[9]

applied for the final model fits. The elastic dry friction model is the only Masing WJROM model to use quadrature integration (51 quadrature points between amplitude levels) to calculate dissipation (see Section 3.4). The modal level quadrature integration scheme introduces negative dissipation[8] at low amplitude levels (e.g., see elastic dry friction in Table 5), but this behavior becomes less severe for increasing numbers of quadrature points. The local analytical dissipation calculation used for most models does not show this behavior, so only elastic dry friction is affected by the low amplitude negative dissipation.

The first two models, Jenkins and elastic dry friction, produce the worst model fits (highest errors) for the first mode. This is expected since both models are generally formulated to be used with more DOFs such as the FJROM. The inclusion of a post-slip stiffness in the Prager and Generalized Jenkins Prager models appears to improve the flexibility slightly, allowing these models to achieve lower damping errors. The Generalized Jenkins Prager model has the most parameters and achieves the lowest errors of these four models. The success of the Prager model compared to the Jenkins model suggests that the tangential stiffness $k_t$is minimally important for model fitting flexibility.

All of the bilinear friction models show an abrupt increase in damping when the joint starts to slip (e.g., see the examples provided in Table 5 for the Jenkins, Elastic Dry Friction, and Generalized Jenkins Prager models). This results in relatively high damping errors for these models since they cannot capture the smooth experimental dissipation trend. The inability of the bilinear friction models to capture the gradual increase in the damping factor motivates the use of microslip models.

The first two microslip models, the 4- and 5-parameter Iwan models, produce nearly identical Pareto fronts and achieve significantly lower damping and frequency errors than the bilinear friction models. The lower errors can be attributed to the ability of the models to smoothly vary the frequency and damping factor (e.g., see Fig. 7 for example backbones for the 4-parameter Iwan model). The two Iwan models behave similarly because the parameter θ in the 5-parameter Iwan model generally converged to values near 1, thus approaching the case of the 4-parameter Iwan model. Also of interest, β converged to values close to zero (see Section A for parameter ranges) corresponding to a smooth force–displacement relationship at the transition to macroslip. While $\theta = 1$ and $\beta = 0$ may be reasonable for the current data set, this may not generally hold for joints that slip more than the present experimental data set such as those described in [1,12].

Though the initially proposed Iwan model limits the parameter $\chi \in (-1, 0]$ based on experimental observations [4], the model fitting was conducted allowing $\chi \in [-2, 2]$ and $\chi \in [-2, 1]$ for the 4- and 5-parameter Iwan models respectively. Since the power law dissipation in the microslip regime is $\chi + 3$, values of χ approaching -2 and -1 correspond to dry friction and viscous dissipation trends respectively. All Pareto optimal parameter sets satisfied the originally proposed lower bound of $\chi > -1$, indicating that the model fits require greater damping than can be provided with either dry friction or viscous damping. The single and two points with the lowest damping errors for the 4- and 5-parameter Iwan models respectively have values of $\chi > 0$, so it is useful to relax the proposed upper limit on χ to allow greater model flexibility.

Next, three variations of the Bouc-Wen model without a post-slip stiffness are considered. The general Bouc-Wen model produces the lowest errors of the microslip models, including the more popular Iwan models. However, the general Bouc-Wen model may be undesirable because of the additional computational cost of numerically integrating the force–displacement relationship (see Section 2.3.2). The Bouc-Wen $n = 1$ model provides a reasonable (in terms of errors) and computationally cheaper alternative for the damping optimized portion of the Pareto fronts where the general model converged to values of n close to 1. The Bouc-Wen $n = 2$ model has the highest damping errors of the microslip models, but still improves on the simpler bilinear models.

The last three models (Valanis, Bouc-Wen $n = 1$ with a post-slip stiffness, and 4-Parameter Iwan with a post-slip stiffness) all include a post-slip stiffness parameter. The Valanis model and the Bouc-Wen $n = 1$ with the post-slip stiffness model show nearly identical Pareto fronts because the Valanis model converges to values of κ close to zero, which matches the Bouc-Wen $n = 1$ with a post-slip stiffness model for the case of monotonic loading. However, the Valanis model is more expensive computationally due to the numerical integration of the force–displacement relationship. Furthermore, the Valanis model and the Bouc-Wen $n = 1$ with post-slip stiffness model show no distinguishable improvement compared to the Bouc-Wen $n = 1$ model (without a post-slip stiffness). Conversely, the 4-parameter Iwan with a post-slip stiffness model shows some improvement over the other Iwan models for the

---

[8] Viscous damping is added at all amplitude levels, so the total damping factor remains positive.

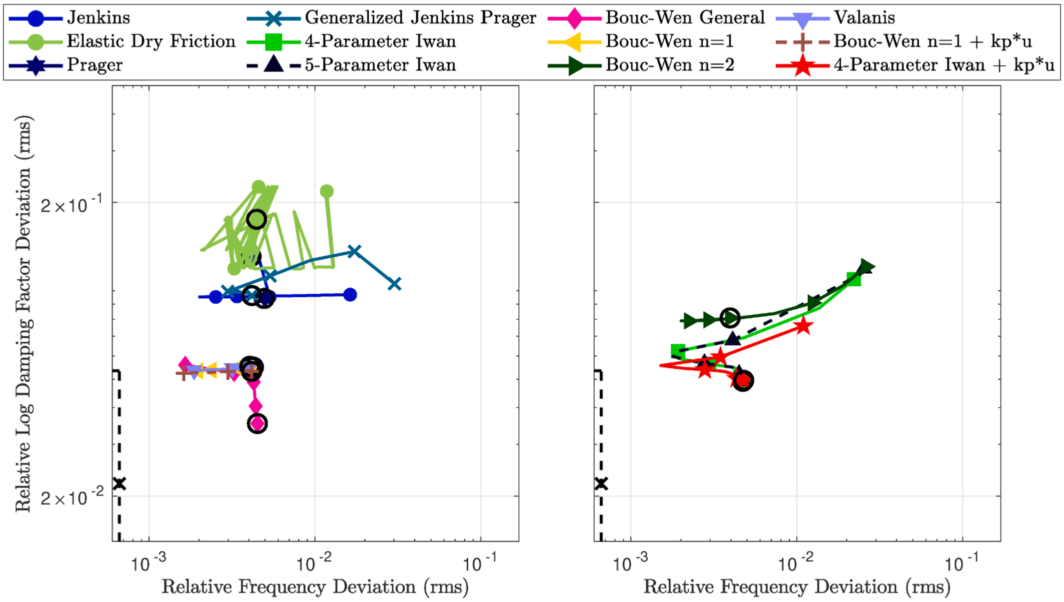

Fig. 11. Masing WJROM errors for mode 1 designs applied to mode 2. The y-axis is shared. The dashed box represents experimental variability and the black x is the reference point for calculating the quantitative measure of epistemic uncertainty. Black circles indicated the optimal design for mode 1 frequency. The data is plotted in separate figures for clarity.

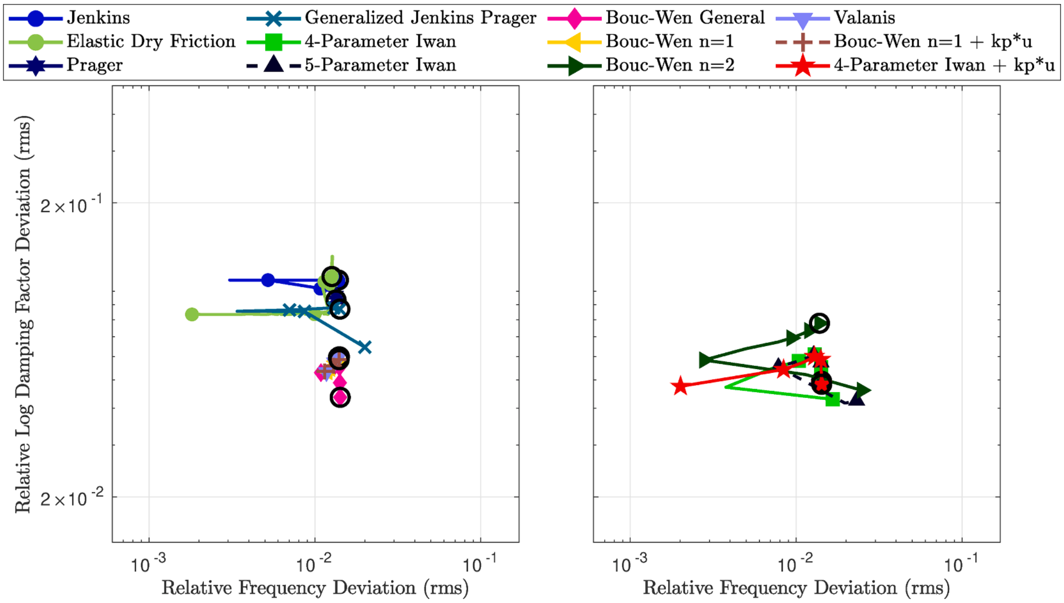

Fig. 12. Masing WJROM errors for mode 1 designs applied to mode 3. The y-axis is shared. The experimental variability and the reference point for calculating the quantitative measure of epistemic uncertainty fall outside of the plot bounds. Black circles indicated the optimal design for mode 1 frequency. The data is plotted in separate figures for clarity.

damping optimized portion of the Pareto front.

For the models with a post-slip stiffness, the parameter ranges (see Section A) suggest that for many cases the post-slip stiffness has little effect on the simulations. For the Valanis model, the post-slip stiffness ranges from 1.02e−7 to 5.92e−3 times the tangential stiffness. For the Bouc-Wen $n = 1$ with a post-slip stiffness model, the post-slip stiffnesses ranges from 2.91e−3 to 5.96e−3 times the tangential stiffness. These small values, likely have little effect on the overall dynamics of the system. Similarly, the point with the lowest frequency error for the 4-parameter Iwan with a post-slip stiffness model has a post-slip stiffness that is over nine orders of magnitude smaller than the tangential stiffness of that parameter set. On the other hand, the damping optimized points have more notable values of the post-slip stiffness that are up to 8% of the tangential stiffness.

Table 6
Non-Masing WJROM simulation options.

Model	Penalize Residuals	Number of Loops	ζ Convergence Tolerance	Conservative Prestress
Jenkins	Yes	3	1e−4	No
Elastic Dry Friction	Yes	6	1e−4	No
Bouc-Wen $n = 1$	Yes	40	1e−4	Yes
Valanis	No	40	1e−4	Yes
Bouc-Wen $n = 1+$ kp*u	No	100	1e−4	Yes

The general Bouc-Wen model and the three Iwan models all produce similar minimum frequency and damping errors. Since the end points of the Pareto fronts may not be fully achieved with the current optimizations, it cannot be concluded if one of these provides the best option for either individual error metric. However, the general Bouc-Wen model does the best job of simultaneously obtaining low frequency and damping errors.

Table 5 includes three example backbones for the Valanis model, all of which show trends very similar to the experimental data. Furthermore, the model is able to capture the smooth variations in damping and frequency unlike the bilinear models. All of the microslip models achieve at least a single point with frequency and damping errors less than the experimental variability (dashed box in the lower left of Fig. 9). The damping optimized backbone for the Valanis model (see Table 5) shows that most of the error is in the low amplitude regime. This is consistent with the high variability in the experimental data in the same regime (see Fig. 3), suggesting that the error may be predominately due to experimental variability. However, some models (e.g., the general Bouc-Wen model) are more flexible and therefore better able to fit (and potentially overfit) the experimental data.

The boundary intersection and genetic algorithm optimization methods are compared in Fig. 10 for the 4-parameter Iwan model and find nearly identical Pareto fronts. The differences on the ends of the Pareto fronts are expected since neither method can guarantee that the full extent of the Pareto front is found. Furthermore, the only notable difference between the parameter ranges (see Section A) is the normal stiffness. This is likely because the boundary intersection method makes use of gradient information to push parameters to the most optimal values. On the other hand, the genetic algorithm converges when the errors remain within a tolerance and thus produces less extreme values of parameters when the sensitivity of the errors to a parameter is low. The consistency of the two optimization methods suggests that Pareto fronts obtained by both methods can be compared throughout this paper. The results throughout the rest of this paper only refer to the boundary intersection results produced by the 4-parameter Iwan model.

4.1.2. Modes 2 and 3

After fitting to the mode 1 experimental data, the Pareto optimal parameters of each model are applied to the second and third bending modes (Figs. 11 and 12 respectively). Many of the parameters applied to the higher modes show lower frequency error because the higher modes behave more linearly over the amplitude range measured. Consequently, even linear predictions of the response (such as the Jenkins model parameters applied to mode 3 in Table 5) result in similar errors. The low errors for the higher modes are in contrast to previous calibration efforts in which very poor estimates of the higher modes were achieved [7], and is at least partly attributable to the preservation of local kinematics in the reduced order modeling framework [44].

The bilinear friction models (Jenkins, elastic dry friction, Prager, Generalized Jenkins Prager) show comparable frequency errors but higher damping errors than the other model parameter sets applied to the second and third modes. This is expected since the models are not able to capture the smooth damping transitions.

For both higher modes, the 4- and 5-parameter Iwan models show identical behavior with small variations due to the exact positioning of points on the mode 1 Pareto front. In these models, a point towards the middle of the first mode Pareto fronts results in the lowest frequency error for the second and third modes. The frequency optimized points for mode 1 produce the lowest damping errors for mode 2 while the damping optimized points for mode 1 produce the lowest damping errors for mode 3. Overall, this behavior suggests that a point from the middle of the mode 1 Pareto front may be a good choice for high modes, possibly because balancing mode 1 frequency and damping fits limits model overfitting. As with mode 1, the 4-parameter Iwan with post-slip stiffness model shows similar behavior to the other two Iwan models with slight variations for the mode 1 damping optimized parameter sets.

The general Bouc-Wen model produces the lowest damping errors for mode 2 and frequency errors comparable to the other microslip models. The two Bouc-Wen $n = 1$ models and the Valanis model show comparable errors to the 4- and 5-parameter Iwan models for the higher modes. As with mode 1, these three models all produce very similar results since the frictional loading curves are nearly identical for the optimized parameters. The Bouc-Wen $n = 2$ model performs worse than the other microslip models, but shows similar behavior to the Iwan models where a parameter set from the middle of the mode 1 Pareto front produces the best frequency results for the higher modes.

---

[9] Here, only the results from the last generation of the genetic algorithm are plotted. This gives slightly higher errors than the procedure of using the last 50 generations for the genetic algorithm, which is used for all other genetic algorithm optimizations. Thus, the present figure shows a worst case comparison between the genetic algorithm and the boundary intersection methods.

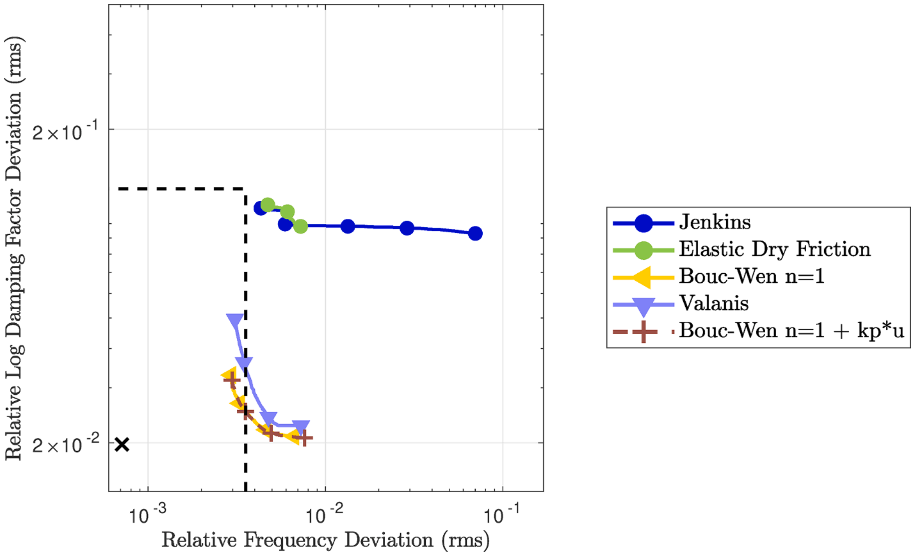

Fig. 13. Non-Masing WJROM Pareto fronts for mode 1. The dashed box represents experimental variability and the black x is the reference point for calculating the quantitative measure of epistemic uncertainty.

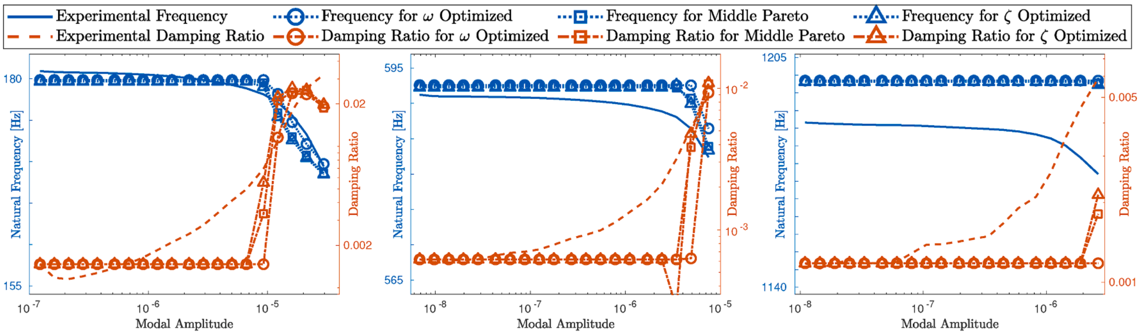

(a) (b) (c)

Fig. 14. Backbone plots for WJROM non-Masing elastic dry friction for (a) first, (b) second, and (c) third modes.

4.2. *WJROM non-Masing*

Following the Masing simulations, the Jenkins, elastic dry friction, Bouc-Wen $n = 1$, Valanis, and Bouc-Wen $n = 1$ with post-slip stiffness models are investigated with the WJROM in a non-Masing framework. This section presents more specifics of the modeling procedure, mode 1 optimized results, and errors for the mode 1 parameters applied to the second and third modes.

4.2.1. *Modeling considerations*

As mentioned in Section 3.5, the current implementation of boundary intersection did not converge for the non-Masing simulations, so the genetic algorithm was used to produce all of the Pareto fronts. The initial fits of some models yielded high residuals for the nonlinear RQNMA solutions (see Section 3.4), thus the residual penalization scheme (see Section 3.5.2) was used for these models (see Table 6).

As mentioned in Section 3.4, the hysteresis loops are repeated as necessary to obtain closed hysteresis loops (see Table 6). Relatively few repetitions are used for the Jenkins and elastic dry friction models, since the slider representations are expected to rapidly converge to a constant dissipation. Based on initial tests, more repetitions of the hysteresis loop are allowed for the three microslip models. In addition, if the fractional change in damping between two iterations (calculated as $|\zeta_n - \zeta_{n-1}|/\zeta_n$) is less than a tolerance of 1e−4, then the damping calculation is terminated before completing the maximum number of loops. Finally, the variants of the Bouc-Wen model and the Valanis model are calculated with the conservative prestress method described in Section 3.3 since the method converged more rapidly to closed hysteresis loops and was more consistent with single degree of freedom frequency domain simulations.

The dissipations for the Jenkins, two variants of the Bouc-Wen, and Valanis models are all calculated analytically using local

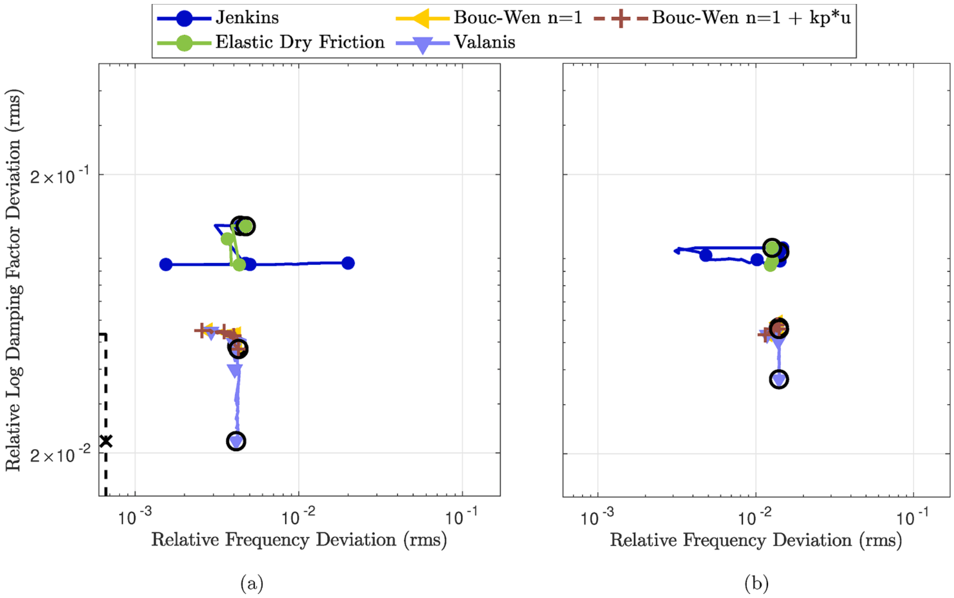

Fig. 15. Non-Masing WJROM errors for mode 1 designs applied to (a) mode 2 and (b) mode 3. The y-axis is shared. For mode 2, the dashed box represents experimental variability and the black x is the reference point for calculating the quantitative measure of epistemic uncertainty. For mode 3, the experimental variability and the reference point fall outside of the plot bounds. Black circles indicated the optimal design for mode 1 frequency.

force–displacement relationships. The elastic dry friction model uses 41 quadrature points (see Section 3.4) per unloading or loading segment of the global hysteresis loop. Fewer quadrature points are used than for the Masing elastic dry friction model, because the non-Masing case does not have the issue of negative dissipation at low amplitudes for low numbers of quadrature points.

To eliminate residual penalization and to store additional information about the backbone curves, the parameter sets found through optimization are rerun through the error calculation. In some cases, the recalculated errors are slightly different than the results outputted from the genetic algorithm (possibly due to differences in the convergence of the nonlinear solutions when running on different hardware). Of the WJROM Masing and non-Masing simulations, only the non-Masing Bouc-Wen $n = 1$ and non-Masing Valanis models showed notable changes with 1 of 131 and 8 of 111 Pareto optimal parameter sets respectively yielding errors (of the log mean-squared error or (42)) that increased from the initial calculation by between 0.06 and 0.18. This results in a relatively small change in the errors for only a small fraction of the plotted values. In addition, only the Pareto optimal set of the recalculated errors is plotted.

4.2.2. Mode 1

The Pareto fronts for the non-Masing WJROM models are shown in Fig. 13. As with the Masing WJROM optimizations, the microslip models achieve errors less than the experimental variability while the bilinear models have higher frequency errors.

The optimization of the non-Masing Jenkins model resulted in a Pareto front that is indistinguishable from the Masing Pareto front. The parameter ranges between the Masing and non-Masing cases are similar (see Section A for parameter ranges), but all of the Masing optimized parameter sets have either k_t or k_n larger than the maximum values for the non-Masing case. Since the Pareto fronts are indistinguishable, it is likely that the sensitivity to these parameters is too small for the genetic algorithm to identify parameter sets with the higher values of k_t or k_n. On the other hand, the boundary intersection method for the Masing case makes use of gradient information, so it can push parameters to extreme values even if the changes in error are very small. The consistency of the two Jenkins Pareto fronts suggests that the Masing assumptions are valid for the Jenkins model (as expected) and that the two optimization methods provide comparable results (as also shown in Fig. 10).

Unlike the Jenkins model, the elastic dry friction model produces a somewhat different Pareto front between the Masing (see Fig. 9) and non-Masing (see Fig. 13) frameworks with slightly higher damping errors for the non-Masing case. For the non-Masing case, the backbone plots (see Fig. 14) show a clear decrease in damping factor after the initial increase due to the onset of slip in contrast to the Masing case (see Table 5) where the damping factor continues to increase after the onset of slip. Furthermore, about half of the Masing optimized parameter sets have a friction coefficient larger than the maximum value of the non-Masing optimized parameter sets. The discrepancies between the Masing and non-Masing frameworks imply that under more realistic, non-monotonic loading conditions (e.g., in time or frequency domain simulations), the model fits generated based on the Masing assumptions will likely contain higher errors than predicted by the Masing RQNMA framework.

The Pareto fronts for the non-Masing Bouc-Wen $n = 1$ with and without post-slip stiffness models are notably different from the Masing case. For the non-Masing case, both models behave the same but have higher damping errors, especially for the frequency optimized points, compared to the Masing case. The Valanis model shows similar behavior to the Bouc-Wen $n = 1$ models, but with

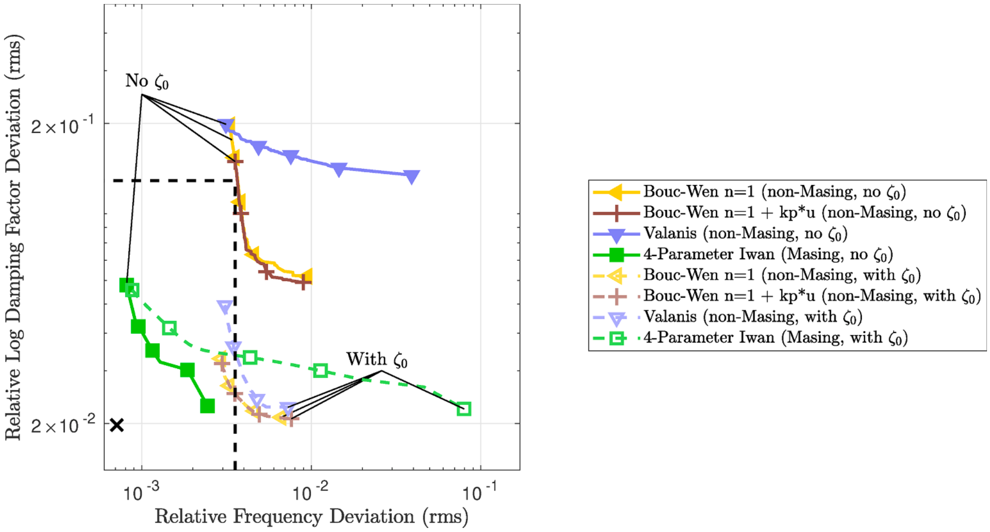

Fig. 16. WJROM Pareto Fronts for mode 1, without viscous damping. The dashed box represents experimental variability and the black x is the reference point for calculating the quantitative measure of epistemic uncertainty.

Table 7

Backbone plots for different WJROMs without viscous damping. The damping ratio ranges for individual models are modified here compared to other backbone plots to show the small amounts of damping at low amplitudes.

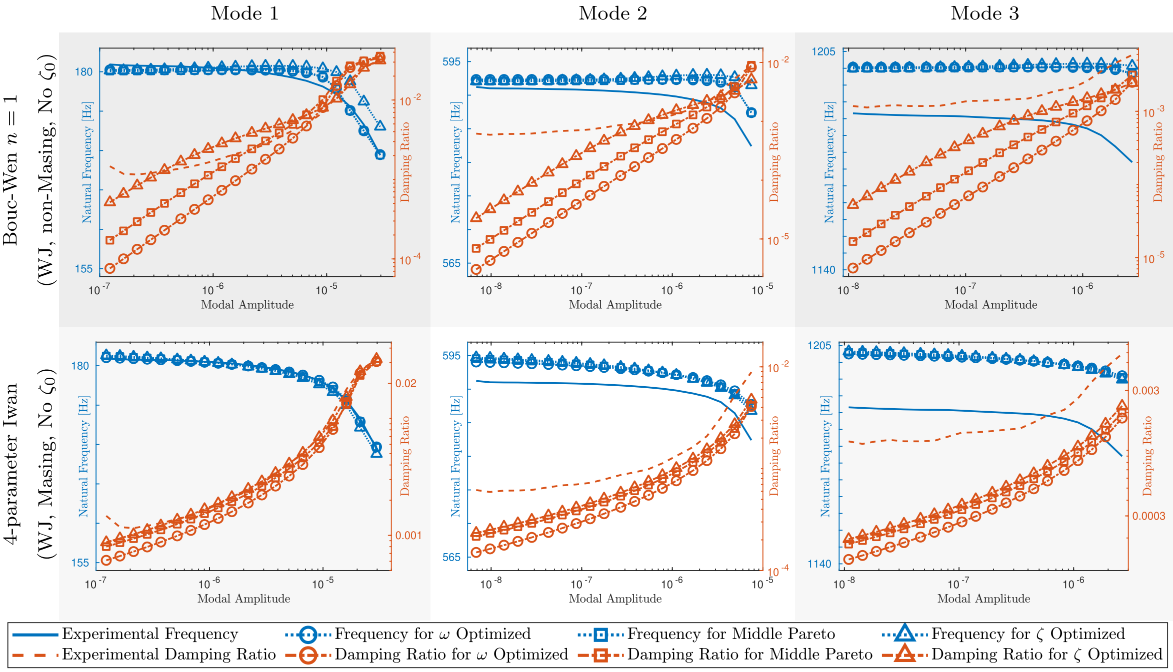

higher damping errors. This differs from the Masing case where the three models had nearly identical Pareto fronts.

The results show similar behavior for the one Masing model, Jenkins, that is compared between the Masing and non-Masing frameworks. On the other hand, the results show clearly different behavior for the elastic dry friction, Bouc-Wen $n = 1$, Valanis, and Bouc-Wen $n = 1$ with a post-slip stiffness models between the Masing and non-Masing cases. This can be interpreted as showing that these models should be considered within a non-Masing framework to assess how they would behave in time or frequency domain simulations. If these models are optimized using a Masing framework, then subsequent time or frequency domain simulations will have different stiffness and dissipation properties, introducing unaccounted for errors into the optimized system models.

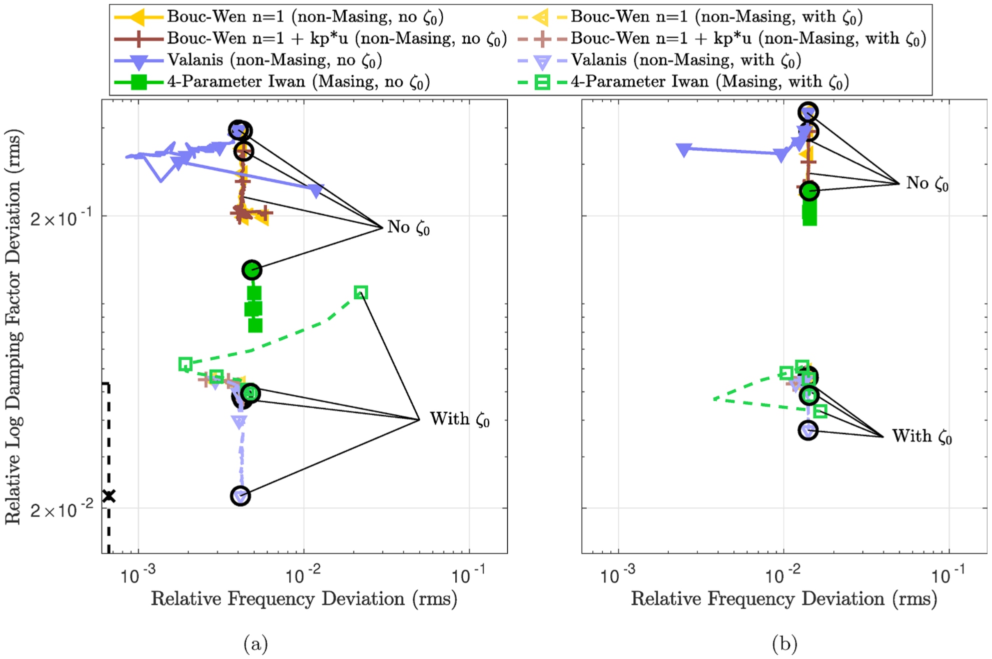

Fig. 17. WJROM errors for mode 1 designs without viscous damping applied to (a) mode 2 and (b) mode 3. The y-axis is shared. For mode 2, the dashed box represents experimental variability and the black x is the reference point for calculating the quantitative measure of epistemic uncertainty. For mode 3, the experimental variability and the reference point fall outside of the plot bounds. Black circles indicated the optimal design for mode 1 frequency.

4.2.3. Modes 2 and 3

The errors calculated from the optimized mode 1 parameters applied to the second and third bending modes for the non-Masing WJROM are shown in Fig. 15. For the Jenkins and elastic dry friction models, the non-Masing and Masing results are similar for the second and third modes. For the elastic dry friction backbone in Fig. 14, one of the mode 2 points has a sudden decrease in damping before slipping caused by high residuals in the RQNMA solution at $-q$ at that amplitude. Since this is isolated to a single amplitude level, it does not significantly impact the mode 2 errors plotted here.

For modes 2 and 3, the two Bouc-Wen $n=1$ models and the Valanis model show similar trends to the Masing case. In addition, the Valanis model shows a branch for the higher modes with notably lower damping errors than the Masing case. Furthermore, besides for the low damping error branch for the Valanis model, the Bouc-Wen $n=1$ models and the Valanis model behave similarly for modes 2 and 3 despite the differences for the non-Masing mode 1 Pareto fronts.

4.3. WJROM without viscous damping

Often with model fitting, viscous damping is added to account for the low amplitude damping in experimental data [43,6]; however, even at low amplitudes, jointed structures exhibit more damping than monolithic structures. Low amplitude tests show that monolithic structures only have damping factors of around 30–65% of those of jointed structures [2,22,62]. This section explores the ability of four microslip models (the non-Masing versions of the Bouc-Wen $n=1$ model, the Valanis model, and the Bouc-Wen $n=1$ with post-slip stiffness model, and the Masing 4-parameter Iwan model) to capture the full damping behavior of the structure without any linear damping contributions. None of the bilinear friction models are considered because they can not generally give rise to any damping at low amplitude levels. The modeling procedures for these models are the same as for the versions with viscous damping presented in Sections 4.1 and 4.2, except that viscous contributions are not added to the frictional dissipation from Section 3.4.

4.3.1. Mode 1

Fig. 16 shows the Pareto fronts produced for mode 1 without viscous damping. Unlike the cases with viscous damping, several of the models now produce errors higher than the experimental variability.

The Bouc-Wen $n=1$, the Bouc-Wen $n=1$ with post-slip stiffness, and the Valanis models all show similar frequency errors to the case with viscous damping, but significantly higher damping errors. This is expected since the frequency behavior of the models is unchanged, and the model fitting is more difficult because low amplitude damping is not provided. Backbone plots (e.g., see the non-Masing Bouc-Wen $n=1$ model without viscous damping in Table 7) illustrate that these models are unable to capture the qualitative shape of the damping backbone while providing sufficient low amplitude damping.

For the Bouc-Wen $n=1$ model, the damping plot for the parameter set with the lowest damping error has around a third of the

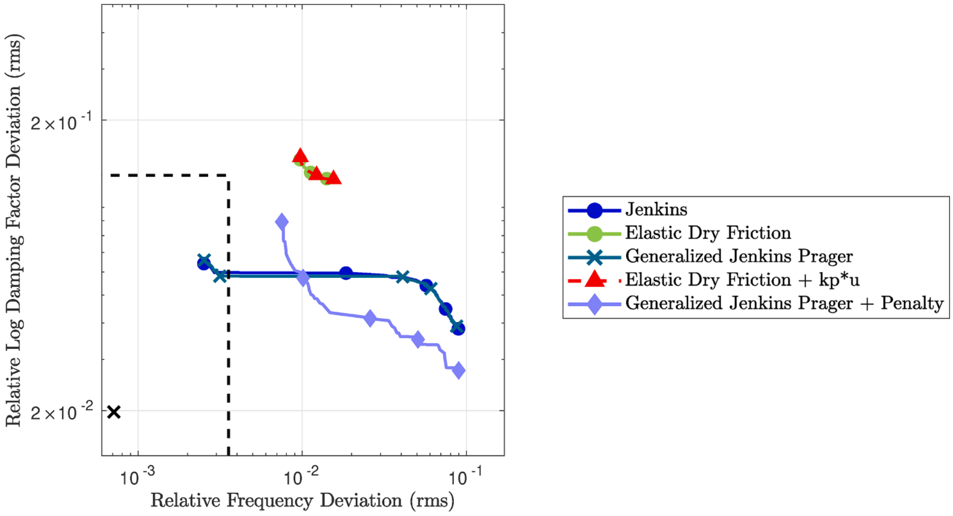

Fig. 18. FJROM Pareto Fronts for mode 1. The dashed box represents experimental variability and the black x is the reference point for calculating the quantitative measure of epistemic uncertainty.

Table 8

Backbone plots for different FJROM non-Masing models. For the Jenkins model, all frequency and the mode 3 damping plot bounds are expanded compared to other models to show Pareto optimal solutions with lower frequency and higher damping factors.

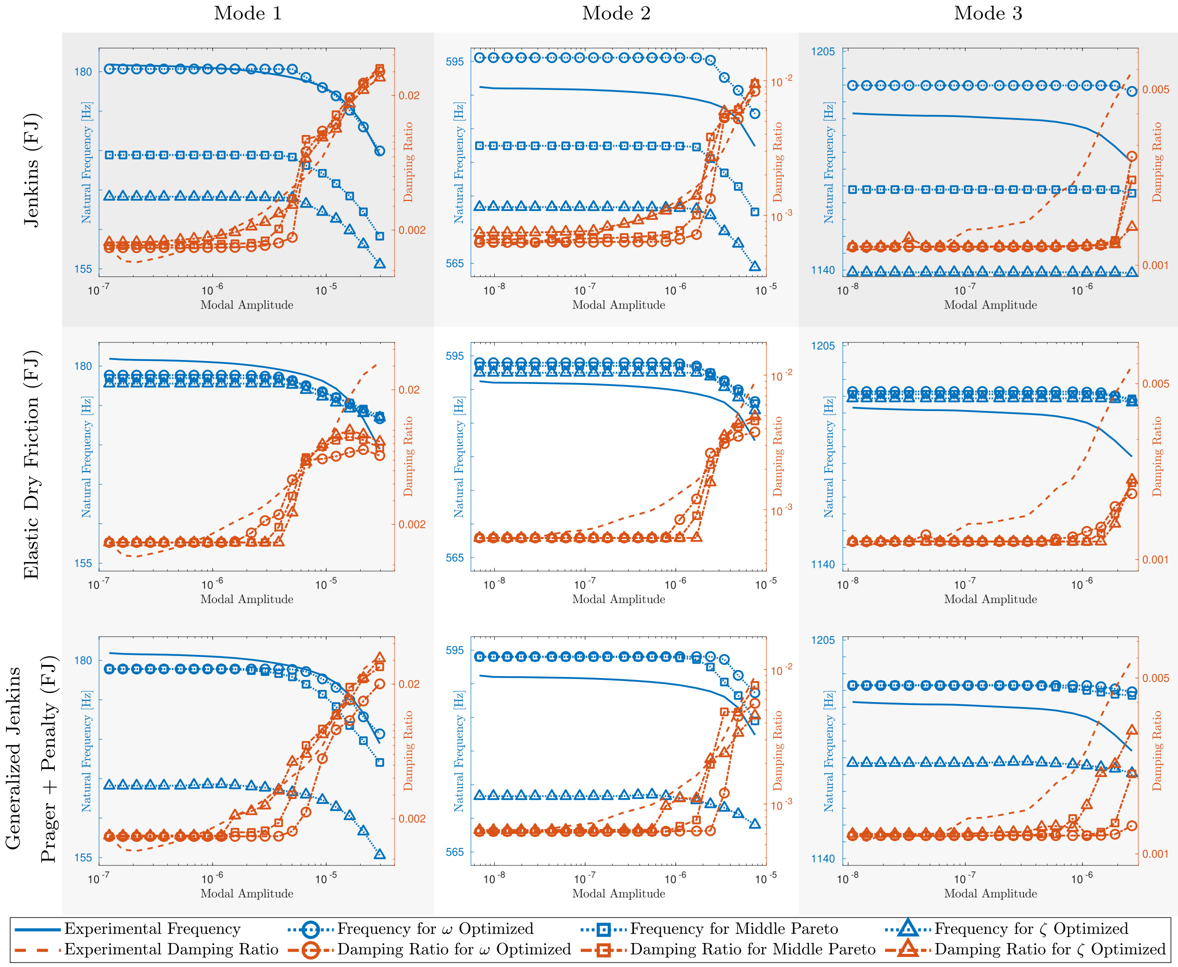

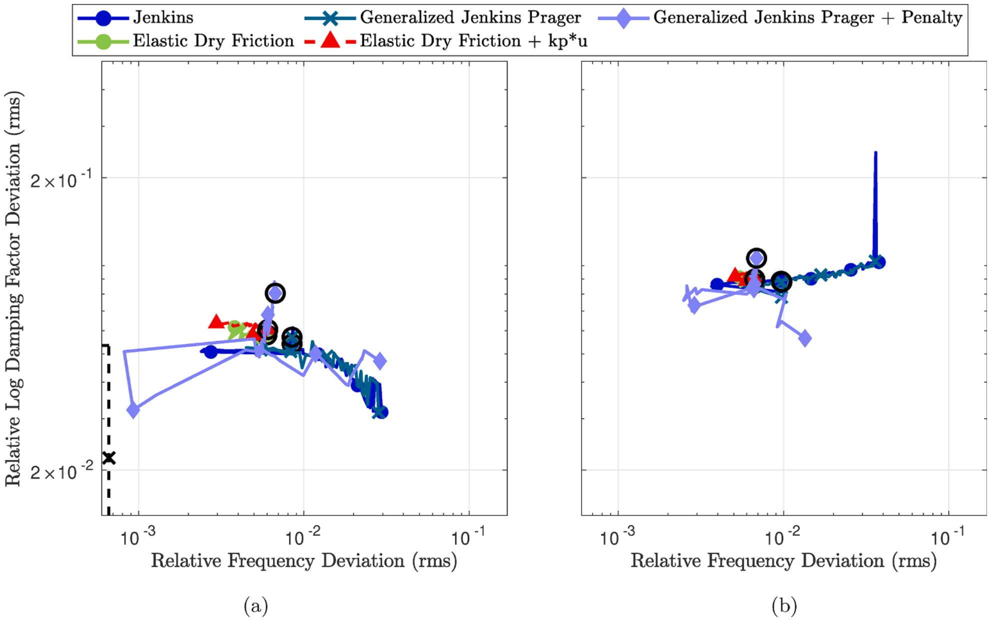

Fig. 19. FJROM errors for mode 1 designs applied to (a) mode 2 and (b) mode 3. The y-axis is shared. For mode 2, the dashed box represents experimental variability and the black x is the reference point for calculating the quantitative measure of epistemic uncertainty. For mode 3, the experimental variability and the reference point fall outside of the plot bounds. Black circles indicated the optimal design for mode 1 frequency.

experimental damping at the lowest amplitude. Adding viscous damping on the order of a monolithic structure may allow the Bouc-Wen $n = 1$ model to achieve the lowest amplitude damping for the parameters of the damping optimized point, but the shape of the damping backbone for that case is qualitatively different than that of the experimental data.

Unlike the previous cases with viscous damping, the Valanis model has significantly higher damping errors than the two Bouc-Wen $n = 1$ models when viscous damping is not used. When recalculating errors for the Valanis model, 7 out of 71 Pareto optimal points had errors change by 0.06 to 0.42 (of the log mean-squared error or (42)). After recalculating errors, any solutions that are not Pareto optimal were removed. Of the remaining 62 points on the Pareto front, 5 had high residuals for the nonlinear RQNMA solution suggesting that there may be some error. Since only a few points on the Pareto front are affected, these errors are not expected to significantly impact the conclusions of this section.

Unlike the three non-Masing models, the Pareto front of the Masing 4-parameter Iwan model without viscous damping shows improvement over the case with viscous damping. At low amplitudes, the case without viscous damping produces between 42–59% of the experimental damping (e.g., see the 4-parameter Iwan model without viscous damping in Table 7), which is consistent with expected frictional damping contributions. In addition, unlike the Bouc-Wen $n = 1$ case, the damping optimized fits for the 4-parameter Iwan model follow the qualitative shape of the experimental damping backbone.

4.3.2. Modes 2 and 3

Fig. 17 shows the errors for the mode 1 optimized parameters applied to modes 2 and 3 without viscous damping. All of the models have higher damping errors than the cases with viscous damping. The two Bouc-Wen models show similar frequency errors to some portions of the viscous damping plots, but significantly higher damping errors. The mode 2 results for the Valanis model include a single point with a negative damping value at one amplitude (treated as 100% error for that amplitude level). Otherwise the model consistently converged, achieving some lower frequency errors than the case of with viscous damping. The 4-parameter Iwan model without viscous damping achieves similar frequency errors to the case with viscous damping for both modes, and similar damping errors for some mode 2 points. However, the damping errors for the case without viscous damping are significantly higher for mode 3. The mode 2 results without viscous damping are noteworthy since the model achieves these by approximating both the low amplitude damping and the shift in damping whereas the case with viscous damping only needs to capture the damping shift.

4.4. FJROM results

4.4.1. Modeling considerations

All of the FJROM models are considered in the non-Masing framework, requiring that the hysteresis loops are repeated until they are closed. Because of the computational cost of the FJROM, all models use a maximum of three repetitions of the hysteresis loop with four quadrature points per loading or unloading segment (see Section 3.4). Any errors due to the quadrature accuracy and imperfectly closed hysteresis loops are sufficiently small for comparing the FJROM models.

For the models with penalty contact (elastic dry friction, elastic dry friction with a post-slip stiffness, and Generalized Jenkins

Table 9
Full ranking of considered models by quantitative measure of epistemic uncertainty. The cells are colored by area fraction on the same scale for all columns.

	Mode: Area Fraction (Ranking)			
Model Name	Average 2,3	1	2	3
Generalized Jenkins Prager + Penalty (FJ, non-Masing)	0.0555 (1.)	0.0651 (14.)	0.0220 (2.)	0.0890 (4.)
Valanis (WJ, non-Masing)	0.0583 (2.)	0.0202 (11.)	0.0137 (1.)	0.1028 (6.)
4-Parameter Iwan + kp*u (WJ, Masing)	0.0656 (3.)	0.0063 (2.)	0.0624 (6.)	0.0687 (1.)
4-Parameter Iwan (WJ, Masing)	0.0666 (4.)	0.0109 (8.)	0.0639 (9.)	0.0694 (2.)
Bouc-Wen General (WJ, Masing)	0.0723 (5.)	0.0005 (1.)	0.0341 (4.)	0.1105 (7.)
5-Parameter Iwan (WJ, Masing)	0.0768 (6.)	0.0085 (6.)	0.0630 (8.)	0.0905 (5.)
Jenkins (FJ, non-Masing)	0.0902 (7.)	0.0650 (13.)	0.0338 (3.)	0.1465 (15.)
Bouc-Wen n=1 + kp*u (WJ, non-Masing)	0.0975 (8.)	0.0155 (9.)	0.0627 (7.)	0.1322 (9.)
Generalized Jenkins Prager (FJ, non-Masing)	0.0983 (9.)	0.0654 (15.)	0.0452 (5.)	0.1514 (16.)
Bouc-Wen n=2 (WJ, Masing)	0.0988 (10.)	0.0415 (12.)	0.1260 (16.)	0.0715 (3.)
Bouc-Wen n=1 (WJ, non-Masing)	0.1004 (11.)	0.0157 (10.)	0.0655 (10.)	0.1354 (13.)
Bouc-Wen n=1 + kp*u (WJ, Masing)	0.1006 (12.)	0.0080 (4.)	0.0689 (11.)	0.1323 (10.)
Valanis (WJ, Masing)	0.1028 (13.)	0.0086 (7.)	0.0723 (12.)	0.1333 (11.)
Bouc-Wen n=1 (WJ, Masing)	0.1038 (14.)	0.0082 (5.)	0.0729 (13.)	0.1348 (12.)
Elastic Dry Friction + kp*u (FJ, non-Masing)	0.1187 (15.)	0.2611 (25.)	0.0811 (14.)	0.1563 (17.)
Elastic Dry Friction (FJ, non-Masing)	0.1198 (16.)	0.2623 (26.)	0.0826 (15.)	0.1570 (18.)
Generalized Jenkins Prager (WJ, Masing)	0.1405 (17.)	0.1476 (18.)	0.1670 (21.)	0.1139 (8.)
Jenkins (WJ, non-Masing)	0.1639 (18.)	0.1734 (20.)	0.1567 (18.)	0.1712 (19.)
Jenkins (WJ, Masing)	0.1711 (19.)	0.1746 (21.)	0.1598 (19.)	0.1825 (20.)
Elastic Dry Friction (WJ, Masing)	0.1752 (20.)	0.1760 (22.)	0.2089 (23.)	0.1415 (14.)
Elastic Dry Friction (WJ, non-Masing)	0.1906 (21.)	0.1831 (23.)	0.1667 (20.)	0.2146 (21.)
Prager (WJ, Masing)	0.1955 (22.)	0.1724 (19.)	0.1718 (22.)	0.2192 (22.)
4-Parameter Iwan (WJ, Masing, no ζ_0)	0.2852 (23.)	0.0072 (3.)	0.1516 (17.)	0.4189 (23.)
Bouc-Wen n=1 + kp*u (WJ, non-Masing, no ζ_0)	0.4159 (24.)	0.0979 (16.)	0.3608 (24.)	0.4709 (24.)
Bouc-Wen n=1 (WJ, non-Masing, no ζ_0)	0.4265 (25.)	0.1026 (17.)	0.3735 (25.)	0.4795 (25.)
Valanis (WJ, non-Masing, no ζ_0)	0.5576 (26.)	0.2541 (24.)	0.4717 (26.)	0.6436 (26.)

Prager with penalty contact), every quadrature point must be evaluated for each loop iteration to allow for a consistent calculation of the reestablishment of contact (see Section 2.1). For these models, a damping relative convergence criteria of 1e-4 is checked to determine if the third iteration is necessary. For the models without penalty contact, only the reversal points are calculated for the first two hysteresis loops, so no convergence criteria is applied.

All of the FJROM models use the residual penalization scheme described in Section 3.5.2. This generally resulted in low residuals for the final solutions with only 6 of the 59 Generalized Jenkins Prager points having high residuals for the nonlinear solution. Since only the Generalized Jenkins Prager model was affected by high residuals, and only for a few points, the residual penalization scheme is effective at eliminating non-converged RQNMA solutions from the Pareto fronts.

The Prager model was investigated for the FJROM, but meaningful results were not obtained due to high RQNMA residuals and poor convergence for hysteresis loops closing. The linear regularization parameter could be decreased from that of the WJROM case, but that would require a value close to what is optimal for the Generalized Jenkins Prager model, making the Prager model essentially identical to the Generalized Jenkins Prager model.

The genetic algorithm for the elastic dry friction model with a post-slip stiffness was seeded with 8 solutions from an initial Pareto front of the elastic dry friction model. Initial tests without seeding the genetic algorithm failed to obtain Pareto fronts near the elastic dry friction model without a post-slip stiffness. Since only 8 of the initial 75 members of the genetic algorithm population are seeded,

Table 10
Time for single backbone calculation using parameters from the middle of the Pareto front using an Intel i7-10710U CPU, 1.10 GHz processor with 6 cores and 32 GB of RAM.

Model	Time (seconds)
Jenkins (WJ, Masing)	0.10
Generalized Jenkins Prager (WJ, Masing)	0.10
Prager (WJ, Masing)	0.14
Bouc-Wen $n = 2$ (WJ, Masing)	0.15
4-Parameter Iwan (WJ, Masing, no ζ_0)	0.15
Bouc-Wen $n = 1 \; + $ kp*u (WJ, Masing)	0.16
Bouc-Wen $n = 1$ (WJ, Masing)	0.16
5-Parameter Iwan (WJ, Masing)	0.17
4-Parameter Iwan (WJ, Masing)	0.17
4-Parameter Iwan $+$ kp*u (WJ, Masing)	0.17
Jenkins (WJ, non-Masing)	0.44
Bouc-Wen General with interpolation (WJ, Masing)	0.45
Valanis with interpolation (WJ, Masing)	0.55
Valanis without interpolation (WJ, Masing)	2.0
Bouc-Wen General without interpolation (WJ, Masing)	2.3
Elastic Dry Friction (WJ, Masing)	3.5
Bouc-Wen $n = 1 \; + $ kp*u (WJ, non-Masing)	3.8
Bouc-Wen $n = 1$ (WJ, non-Masing)	4.3
Bouc-Wen $n = 1 \; + $ kp*u (WJ, non-Masing, no ζ_0)	8.1
Bouc-Wen $n = 1$ (WJ, non-Masing, no ζ_0)	9.3
Valanis (WJ, non-Masing)	44
Elastic Dry Friction $+$ kp*u (FJ, non-Masing)	74
Elastic Dry Friction (FJ, non-Masing)	81
Valanis (WJ, non-Masing, no ζ_0)	86
Generalized Jenkins Prager $+$ Penalty (FJ, non-Masing)	150
Generalized Jenkins Prager (FJ, non-Masing)	170
Jenkins (FJ, non-Masing)	170
Elastic Dry Friction (WJ, non-Masing)	740

the genetic algorithm still has sufficient opportunity to search the entire parameter space.

4.4.2. Mode 1

Fig. 18 shows the Pareto fronts for the FJROM models. The Jenkins and Generalized Jenkins Prager models both show significantly lower damping errors and somewhat lower frequency errors than the WJROM cases (see Sections 4.1 and 4.2). The lower damping errors can be attributed to sufficient DOFs in the FJROM to achieve a smooth increase in damping factor (see Table 8). Lower frequency errors for the FJROM models are driven by smoother transitions as the frequency shifts. Unlike the WJROM Masing case, the FJROM Jenkins and Generalized Jenkins Prager models have nearly identical Pareto fronts. This behavior is similar to that of the WJROM Masing microslip models, suggesting that when the friction model can provide a smooth response (either due to the model form for the WJROM or enough DOFs for the FJROM), the post-slip stiffness does not provide a significant benefit.

While the Jenkins and Generalized Jenkins Prager models show clear improvement when used with the FJROM, the elastic dry friction model (see Fig. 18) has significantly higher frequency errors and slightly higher damping errors than the WJROM case (see Fig. 13). This can be attributed to both insufficient frequency drop off and insufficient damping at higher amplitude levels (see Table 8) compared to the WJROM models (see Table 5 and Fig. 14). Due to the poor performance, the model was also considered with a post-slip stiffness yielding an indistinguishable Pareto front. The values of the post-slip stiffness[10] (see Section A) range from 7.46e−2 to 5.95e−12 times the values of the post-slip stiffness for the FJROM Generalized Jenkins Prager model, and have little to no effect on most of the simulations. Since the post-slip stiffness does not improve either the FJROM Jenkins or the FJROM elastic dry friction models, the post-slip stiffness does not appear to be a valuable feature to include in the FJROM models.

A Generalized Jenkins Prager with penalty contact model is considered as a more physical version of the Generalized Jenkins Prager model. The addition of penalty contact means that all tractions are set to zero when the interface is separated (see Section 2.1), but the model still uses a constant value of the slip traction t_s when in contact rather than a friction coefficient. The Generalized Jenkins Prager with penalty contact model fails to achieve the low frequency errors of the Jenkins and Generalized Jenkins Prager models, but does achieve lower damping errors for some points. This highlights how the models that are expected to be more physical do not necessarily produce better model fits.

4.4.3. Modes 2 and 3

Applying the parameters from the Pareto fronts for mode 1 to modes 2 and 3 yields the errors plotted in Fig. 19. For the mode 3

---

[10] A lower limit of $k_p = 1$ N/m^3 is applied since the parameter is on log-scale and values approximately 12 orders of magnitude smaller than those for the tangential stiffness k_t are expected to have little to no effect on the backbone.

Jenkins model, the single point with the highest damping error is related to a non-converged solution yielding negative damping, and thus being treated as 100% error for that amplitude level.

The FJROM Jenkins model applied to higher modes (see Fig. 19) is similar in terms of frequency error to the WJROM non-Masing case (see Fig. 15). In terms of damping errors compared to the WJROM non-Masing case, the FJROM model has lower errors for mode 2 and similar errors for mode 3. The Generalized Jenkins Prager model showed near identical behavior to the Jenkins model for the higher modes. This is expected since the mode 1 Pareto fronts are also nearly identical.

The elastic dry friction models achieve similar errors to the Jenkins and Generalized Jenkins Prager models, but with slightly higher mode 2 damping errors. This highlights that even through the elastic dry friction model is the most physical, it is still missing necessary physics, so it does a poor job matching the experimental behavior.

Lastly, the Generalized Jenkins Prager with penalty contact model has lower frequency errors for the higher modes compared to the mode 1 model fits. The model with penalty contact also out performs the Generalized Jenkins Prager model in terms of frequency for mode 2 and both frequency and damping for mode 3 despite having higher frequency errors for mode 1. Unlike the poor results for elastic dry friction, this highlights the benefit of including some more physical features in the friction model (e.g., penalty contact), for predicting the higher modes.

4.5. Full model rankings

Table 9 shows the rankings of all of the friction models investigated using the metric discussed in Section 3.7 with the upper and lower area bounds provided in Table 4. The rankings are similar to the graphical interpretations presented in the previous sections. However, the rankings are not exact since the utopian points (see Section 3.5) of the models are not fully achieved. If a model has low error for mode 1, but relatively large errors for the other modes, it may be concluded that the model is “good” only in the sense of curve fitting input data. For a model to be good overall, it should achieve low errors for all modes indicating that some physics has been consistently captured. The area fractions can also be compared to those calculated for the experimental variability by treating the point with coordinates of the experimental variability point as a Pareto front resulting in an L shaped region. This gives areas of 0.2406 for mode 1, 0.0656 for mode 2 and exactly 0 for mode 3.

The primary ranking of interest in considering epistemic uncertainty is the ability of the model to predict the behavior of the higher modes. The epistemic uncertainty metric averaged between the second and third modes yields the first numerical column of Table 9. From this, the FJROM Generalized Jenkins Prager with penalty contact model produces the best predictions for modes 2 and 3. The WJROM non-Masing Valanis model, the 3 Iwan models, and the General Bouc-Wen model all perform similarly well to the FJROM Generalized Jenkins Prager with penalty contact model. The General Bouc-Wen model and the 4-parameter Iwan with post-slip stiffness model achieve the best and second best rankings for mode 1 respectively.

The FJROM elastic dry friction models (with and without post-slip stiffness) perform worse than all of the WJROM microslip models with viscous damping, but are better at predicting the higher modes than the WJROM bilinear models. Furthermore, these two models rank last for their flexibility to fit the first mode’s experimental behavior and are two of only three models with higher mode 1 areas than the experimental variability point. This highlights that while the elastic dry friction model is expected to be the most physical, it is still missing significant physics.

Of the simulations with viscous damping, the bilinear (Masing and non-Masing) WJROM models perform the worst for the average of modes 2 and 3. This is expected, because the WJROM does not have sufficient DOFs to capture the smooth frequency and damping transitions with the bilinear friction models. As expected, the models without viscous damping perform the worst for the higher modes since they have less information about the experimental data, highlighting the importance of including some viscous damping.

Five of the best six models for predicting modes 2 and 3 and the best 12 models for fitting mode 1 all make use of the WJROM, which has fewer frictional elements than the FJROM. These models can perform significantly better given the smoothly varying force displacement relationships. On the other hand, adding significantly more frictional elements for the FJROM is not always sufficient to recreate the smooth behavior, especially in terms of low amplitude damping factor (e.g., see Fig. 7 versus Table 8). Therefore, it may be beneficial to consider smoother microslip models with the FJROM, though this comes with additional computational cost. On the other hand, the FJROM bilinear models do show an improvement over the WJROM bilinear models for predicting the higher modes, highlighting how the interface can be better represented with more frictional elements.

4.6. Computational time

While it is difficult to directly compare the computational times for the optimization due to variable hardware and different optimization algorithms (i.e., boundary intersection versus genetic algorithm), Table 10 shows the time for individual backbone calculations for the different friction models. All models are timed on the same hardware (Intel i7-10710U CPU, 1.10 GHz processor with 6 cores and 32 GB of RAM) using a Pareto optimal set of parameters from near the middle of the Pareto fronts. Though simulation times vary with different model parameters, the values in Table 10 provide a reasonable comparison of the models. For all of the models, times are averaged over 500 to 750 seconds of repeated simulations with the same parameter set.

The WJROM Masing models are generally the fastest, between 0.1 and 0.2 seconds. The WJROM Masing elastic dry friction model

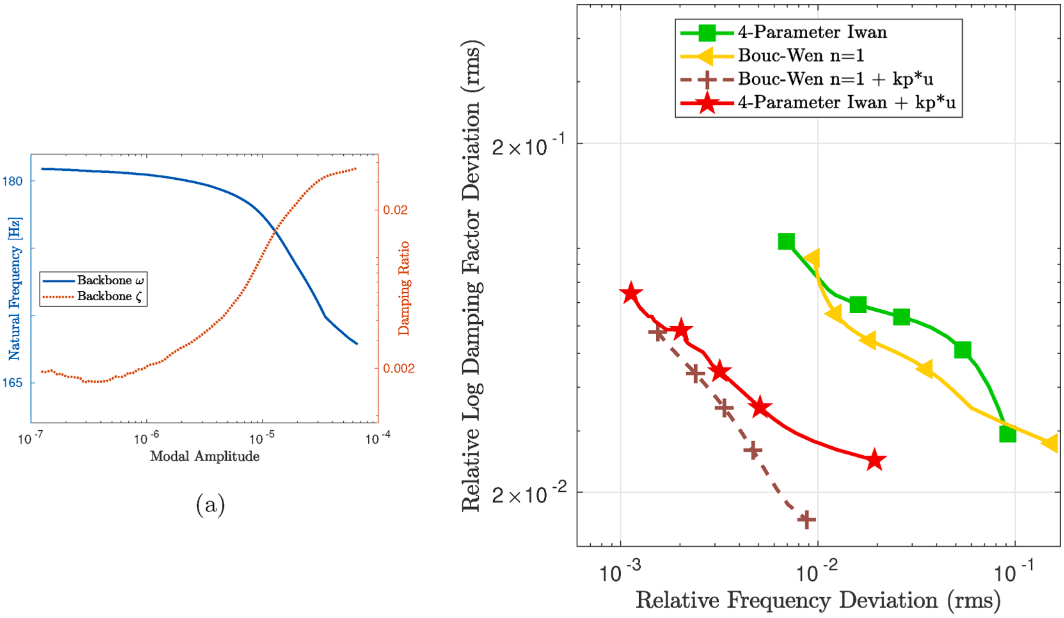

(a)

(b)

Fig. 20. Preliminary results for (a) initial processing of experimental backbone and (b) Masing WJROM models with and without a post-slip stiffness.

takes 3.5 seconds due to the numerical integration of the dissipation (see Section 3.4). The WJROM Masing general Bouc-Wen and Valanis models take 2.3 and 2.0 seconds respectively due to the requirement of numerically integrating the rate form equation to obtain the force for every iteration (see Section 2.3.2). To reduce computational times, these models are also implemented to pre-calculate the force–displacement relationship once for each of the five patches up to an estimated maximum displacement and then interpolate the force for subsequent steps of the RQNMA procedure. This approach (including the initial numerical integration of the force–displacement relationship) gives times of under 0.55 second for both models, but is still slower than other WJROM Masing models. For the timing of the interpolating method, the estimated maximum displacements are the same as those used in the optimization procedure, but are not necessarily the best choice for the specific set of parameters tested. Therefore, faster times may be achievable with the interpolation method, but limitations of accurately predicting the maximum displacements mean that the presented times are a realistic evaluation in a practical setting.

For the WJROM non-Masing models, computational times are higher than the Masing case due to the requirement of repeating the hysteresis loop (see Section 3.4). The WJROM non-Masing elastic dry friction model is the most computationally intensive model due to the numerical integration of the dissipation. The timed parameter set of the elastic dry friction model failed to fully converge for several amplitude levels, likely further increasing the computational time.[11] The Valanis model also takes notably longer than the other WJROM non-Masing models due to the numerical integration of the rate form force–displacement relationship. Unlike the WJROM Masing case, an interpolation scheme did not noticeably speed up simulations since a new numerical integration is required after each reversal point in the hysteresis loop. The WJROM non-Masing models without viscous damping have higher computational times than the variants with viscous damping because more iterations of the hysteresis loop are required to converge the calculated damping factor.

Except for the WJROM non-Masing Valanis model without viscous damping and the non-Masing elastic dry friction model, the FJROM non-Masing models have the highest computation times due to more DOFs, the requirement to repeat hysteresis loops, and numerical integration of dissipation.

4.7. Sensitivity to data

Preliminary model fits used the experimental backbone in Fig. 20a with the WJROM and the Masing framework. Since there was only one experimental trial for the highest data points and the backbone was smoothed, the decrease in slope magnitude above the amplitude of 3e−5 does not accurately reflect the system. However, the resulting model fits are still informative for other systems that

---

[11] The parameter set does converge when run on the hardware for the Pareto fronts and rerunning simulations to save backbone information. However, timing results are run on a different computer to ensure that all models are timed under the same conditions. On the timing computer, the algorithm failed to converge for the elastic dry friction parameter set.

may show similar experimental trends (e.g., those that are transitioning to macroslip).

In Fig. 20b, adding a post-slip stiffness to either the Bouc-Wen $n = 1$ or 4-parameter Iwan models resulted in approximately an order of magnitude decrease in frequency error. This behavior is not observed for the final model fits (see Section 4.1) where the experimental data does not show a change in slope at the highest amplitudes (see Fig. 3). Therefore, if experimental trends show a change in slope at the highest amplitude levels, which is expected when the system enters complete slip, including a post-slip stiffness may become critical to drastically improve a model's ability to fit the experimental data. This behavior was observed for all models considered in this paper with and without a post-slip stiffness except for the FJROM elastic dry friction model that did improve for the preliminary backbone when the post-slip stiffness was added.

5. Conclusions

The major contribution of this paper is evaluating 26 different friction models and discretized representations to evaluate which models have the lowest model form errors. For this, optimized parameter sets and errors are found by solving an multi-objective optimization problem, compared graphically and quantitatively between models, and applied to predict the responses of two other modes. All models show error in both their mode 1 fits and modes 2 and 3 predictions. This error is quantified and used to compare models leading to the conclusions:

- The whole-joint reduced order model (WJROM) with tens of Degrees of Freedom (DOFs) achieves low errors with smooth microslip models. For the full-joint reduced order model (FJROM) with hundreds of DOFs, bilinear friction models can only achieve similar errors to the smooth WJROM models for a few cases. Therefore, it may be beneficial to consider smoother models for the FJROM approach.
- Until an improved or predictive model is proposed, one of the most promising models is the 4-parameter Iwan model (with or without a post-slip stiffness). This model is sufficiently flexible for model fitting, able to predict other modes, and is efficient for the Masing framework due to the analytical solution.
- The WJROM models that are not formulated to follow the Masing hypotheses behave notably different between the Masing and non-Masing frameworks. The Masing model fits of these models should be employed with caution as unaccounted for errors could emerge in time domain or frequency domain simulations due to frictional shakedown and other issues.
- Model fitting with and without viscous damping (to represent material damping of the structure) illustrates that it is paramount to include viscous damping in the model. The 4-parameter Iwan model was better than the Bouc-Wen $n = 1$ (with and without a post-slip stiffness) or Valanis models at producing some damping at the lowest amplitude levels.
- For the FJROM, models that are expected to be more physical are not the best for model calibration of a single mode or predicting higher modes. Therefore, these models are missing important physics.
- For the present data set, a post-slip stiffness does not improve the quality of the model fit. However, for cases where the frequency drop off starts to level off (e.g., at the inception of macroslip), initial results show that it is critical to include a post-slip stiffness in the friction model.

This study has also exposed areas for further development. First, the use of frictional forces in prestress analysis should be evaluated, especially when models show frictional shakedown behavior. There is also room for further development of the quasi-static modal analysis technique employed here (RQNMA) to eliminate the need to repeat the hysteresis loop to converge the damping calculation.

Through assessing a large variety of friction models with different interface representations, this paper highlights the benefits of different friction models and modeling approaches in terms of recreating the behavior of a single mode and predicting the behavior of other modes of a structure.

Declaration of Competing Interest

The authors declare that they have no known competing financial interests or personal relationships that could have appeared to influence the work reported in this paper.

Acknowledgments

Funding: The authors are thankful for the support of the National Science Foundation under Grant No. 1847130. This work was supported in part by the Big-Data Private-Cloud Research Cyberinfrastructure MRI-award funded by NSF under grant CNS-1338099 and by Rice University. This material is based upon work supported by the U.S. Department of Energy, Office of Science, Office of Advanced Scientific Computing Research, Department of Energy Computational Science Graduate Fellowship under Award Number(s) DE-SC0021110. This report was prepared as an account of work sponsored by an agency of the United States Government. Neither the United States Government nor any agency thereof, nor any of their employees, makes any warranty, express or implied, or assumes any

legal liability or responsibility for the accuracy, completeness, or usefulness of any information, apparatus, product, or process disclosed, or represents that its use would not infringe privately owned rights. Reference herein to any specific commercial product, process, or service by trade name, trademark, manufacturer, or otherwise does not necessarily constitute or imply its endorsement, recommendation, or favoring by the United States Government or any agency thereof. The views and opinions of authors expressed herein do not necessarily state or reflect those of the United States Government or any agency thereof.

Appendix A. Model parameter ranges

This section details the ranges of the Pareto optimal model parameters for the friction models described in Section 2 as implemented with logarithmic ($\log_{10}$) and patch area ($\mathscr{A}$) scaling denoted as necessary. Area scaling (see Section 3.2) is removed from the WJROM patch parameters for the values presented in this section such that parameters are directly comparable between the WJROM and FJROM cases. Parameters that are fixed for specific variants of a model (e.g., k_t for Prager and n for some variants of the Bouc-Wen model) are marked in parentheses.

See Tables 11–15.

Table 11

Pareto optimal model parameter bounds (L = Lower, U = Upper) for bilinear friction models with constant slip forces/tractions. All models include viscous damping.

WJROM Parameter:		$\log_{10}(f_s/\mathscr{A})$	$\log_{10}(k_t/\mathscr{A})$	$\log_{10}(k_p/\mathscr{A})$	$\log_{10}(k_n/\mathscr{A})$
FJROM Parameter:		$\log_{10}(t_s)$	$\log_{10}(k_t)$	$\log_{10}(k_p)$	$\log_{10}(k_n)$
Units (Both):		$\log_{10}(\mathrm{N/m^2})$	$\log_{10}(\mathrm{N/m^3})$	$\log_{10}(\mathrm{N/m^3})$	$\log_{10}(\mathrm{N/m^3})$
Jenkins (WJROM, Masing)	L	5.21	12.76	NA	11.32
	U	5.29	17.24	NA	17.76
Jenkins (WJROM, non-Masing)	L	5.18	12.67	NA	11.27
	U	5.28	13.63	NA	16.92
Jenkins (FJROM, non-Masing)	L	5.28	15.12	NA	10.77
	U	5.43	15.52	NA	11.92
Prager (WJROM, Masing)	L	5.25	(18.5)	11.52	12.35
	U	5.26	(18.5)	11.63	12.36
Generalized Jenkins Prager (WJROM, Masing)	L	4.58	11.66	11.12	12.12
	U	5.16	12.79	11.38	18.51
Generalized Jenkins Prager (FJROM, non-Masing)	L	5.27	14.91	9.03	10.79
	U	5.40	15.63	11.23	11.92
Generalized Jenkins Prager + Penalty (FJROM, non-Masing)	L	5.30	13.28	7.43	11.78
	U	5.70	15.52	10.76	13.16

Table 12

Pareto optimal model parameter bounds (L = Lower, U = Upper) for elastic dry friction. All models include viscous damping.

WJROM Parameter:		μ	$\log_{10}(k_t/\mathscr{A})$	$\log_{10}(k_p/\mathscr{A})$	$\log_{10}(k_n/\mathscr{A})$
FJROM Parameter:		μ	$\log_{10}(k_t)$	$\log_{10}(k_p)$	$\log_{10}(k_n)$
Units (both):			$\log_{10}(\mathrm{N/m^3})$	$\log_{10}(\mathrm{N/m^3})$	$\log_{10}(\mathrm{N/m^3})$
WJROM, Masing	L	0.75	12.38	NA	12.28
	U	2.07	14.37	NA	12.33
WJROM, non-Masing	L	0.84	13.83	NA	12.29
	U	1.03	14.96	NA	12.31
FJROM, non-Masing	L	0.65	13.93	NA	11.74
	U	1.47	15.26	NA	11.78
With kp*u, FJROM, non-Masing	L	0.67	13.75	0.00	11.73
	U	1.57	15.5	7.90	11.78

Table 13
Pareto optimal model parameter bounds (L = Lower, U = Upper) for different Masing WJROM Iwan models. The models run with boundary intersection (BI) are used for model comparisons, the genetic algorithm (GA) results are provided solely for comparison between the optimization methods.

		$\log_{10}(f_s/\mathscr{A})$ $\log_{10}(\mathrm{N/m^2})$	$\log_{10}(k_t/\mathscr{A})$ $\log_{10}(\mathrm{N/m^3})$	χ*	$\log_{10}(\beta)$†	θ	$\log_{10}(k_p/\mathscr{A})$ $\log_{10}(\mathrm{N/m^3})$	$\log_{10}(k_n/\mathscr{A})$ $\log_{10}(\mathrm{N/m^3})$
4-parameter, with ζ_0, BI	L	4.94	11.72	−0.84	−6.53	NA	NA	16.29
	U	5.30	13.10	0.09	−3.31	NA	NA	19.17
4-parameter, with ζ_0, GA	L	4.85	11.58	−0.72	−8.64	NA	NA	12.61
	U	5.31	12.97	0.23	−3.02	NA	NA	15.51
4-parameter + kp*u, with ζ_0, BI	L	5.02	12.11	−0.84	−3.76	NA	3.83	14.51
	U	5.30	13.11	0.00	−1.47	NA	11.07	18.50
4-parameter, without ζ_0, BI	L	5.28	13.19	−1.00	−2009.75	NA	NA	13.32
	U	5.32	15.64	−0.88	−3.79	NA	NA	18.42
5-parameter, with ζ_0, BI	L	4.85	11.57	−0.82	−4.84	0.88	NA	13.91
	U	5.30	13.07	0.17	−2.87	1.00	NA	18.40

† $\log_{10}(\beta) < -324$ evaluates to $\beta = 0$ for the present implementation.
* All model fits have values of $\chi > -1$, values are presented rounded to two decimal places.

Table 14
Pareto optimal model parameter bounds (L = Lower, U = Upper) for variants of the Bouc-Wen model.

General:	—	$\log_{10}(A)$ $\log_{10}(\mathrm{N/m^3})$	$\log_{10}(\eta)$ $\log_{10}(\mathrm{N^{1-n}/m^{3-2n}})$			n		$\log_{10}(k_n/\mathscr{A})$ $\log_{10}(\mathrm{N/m^3})$
n = 1:	—	$\log_{10}(A/\mathscr{A})$ $\log_{10}(\mathrm{N/m^3})$	$\log_{10}(\eta)$ $\log_{10}(1/\mathrm{m})$	$\log_{10}(\alpha)$ $\log_{10}(1/\mathrm{m})$	β/α	n	$\log_{10}(k_p/\mathscr{A})$ $\log_{10}(\mathrm{N/m^3})$	$\log_{10}(k_n/\mathscr{A})$ $\log_{10}(\mathrm{N/m^3})$
n = 2:		$\log_{10}(A/\mathscr{A})$ $\log_{10}(\mathrm{N/m^3})$	$\log_{10}(\eta\mathscr{A})$ $\log_{10}(\mathrm{m/N})$			n		$\log_{10}(k_n/\mathscr{A})$ $\log_{10}(\mathrm{N/m^3})$
General, Masing, with ζ_0	L	12.60	6.92	NA	NA	0.50	NA	15.97
	U	12.94	10.29	NA	NA	1.08	NA	18.27
n = 1, Masing, with ζ_0	L	12.67	7.39	NA	NA	(1)	NA	16.18
	U	12.84	7.55	NA	NA	(1)	NA	18.54
n = 2, Masing, with ζ_0	L	11.53	1.81	NA	NA	(2)	NA	17.64
	U	12.78	2.25	NA	NA	(2)	NA	19.33
n = 1+ kp*u, Masing, with ζ_0	L	12.68	7.40	NA	NA	(1)	10.14	13.43
	U	12.83	7.55	NA	NA	(1)	10.59	18.60
n = 1, non-Masing, with ζ_0	L	12.64	NA	7.11	−0.89	(1)	NA	13.96
	U	12.82	NA	7.28	−0.35	(1)	NA	14.88
n = 1+ kp*u, non-Masing, with ζ_0	L	12.62	NA	7.09	−0.77	(1)	8.48	13.82
	U	12.82	NA	7.29	−0.37	(1)	10.26	14.84
n = 1, non-Masing, without ζ_0	L	12.77	NA	7.58	0.08	(1)	NA	13.18
	U	12.84	NA	8.43	0.91	(1)	NA	14.72
n = 1+ kp*u, non-Masing, without ζ_0	L	12.77	NA	7.82	0.45	(1)	6.04	12.87
	U	12.86	NA	8.49	0.91	(1)	10.14	14.75

Table 15
Pareto optimal model parameter ranges for the Valanis model.

		$\log_{10}(E_0/\mathscr{A})$ $\log_{10}(\mathrm{N/m^3})$	$\log_{10}(\lambda)$ $\log_{10}(1/\mathrm{m})$	$\log_{10}(E_t/\mathscr{A})$ $\log_{10}(\mathrm{N/m^3})$	κ	$\log_{10}(k_n/\mathscr{A})$ $\log_{10}(\mathrm{N/m^3})$
Masing, with ζ_0	L	12.66	7.38	5.76	0.00	18.16
	U	12.82	7.53	10.58	0.01	19.88
non-Masing, with ζ_0	L	12.62	7.30	8.65	0.01	13.51
	U	12.81	7.58	11.04	0.34	19.5
non-Masing, without ζ_0	L	12.10	7.13	10.96	0.00	14.18
	U	12.85	7.83	11.76	0.06	21.31

References

[1] D.J. Segalman, D.L. Gregory, M.J. Starr, B.R. Resor, M.D. Jew, J.P. Lauffer, N.M. Ames, Handbook on Dynamics of Jointed Structures. Technical Report SAND2009-4164. Sandia National Laboratories, Albuquerque, NM, 2009.

[2] M.R.W. Brake (Ed.), The Mechanics of Jointed Structures, Springer, 2017.

[3] A.T. Mathis, N.N. Balaji, R.J. Kuether, A.R. Brink, M.R.W. Brake, D.D. Quinn, A review of damping models for structures with mechanical joints, Applied Mechanics Reviews 72 (4) (2020). ISSN 0003-6900.

[4] D.J. Segalman, A four-parameter Iwan model for lap-type joints, Journal of Applied Mechanics 72 (5) (2005) 752–760.

[5] J. Abad, F.J. Medel, J.M. Franco, Determination of Valanis model parameters in a bolted lap joint: Experimental and numerical analyses of frictional dissipation, International Journal of Mechanical Sciences 89 (2014) 289–298. ISSN 0020-7403.

[6] N.N. Balaji, M.R.W. Brake, The surrogate system hypothesis for joint mechanics, Mechanical Systems and Signal Processing 126 (2019) 42–64. ISSN 0888-3270.

[7] R. Lacayo, L. Pesaresi, J. Groß, D. Fochler, J. Armand, L. Salles, C. Schwingshackl, M. Allen, M.R.W. Brake, Nonlinear modeling of structures with bolted joints: a comparison of two approaches based on a time-domain and frequency-domain solver, Mechanical Systems and Signal Processing 114 (2019) 413–438.

[8] G.M. Jenkins, Analysis of the stress-strain relationships in reactor grade graphite, British Journal of Applied Physics 13 (1962) 30–32.

[9] M. Oldfield, H. Ouyang, J.E. Mottershead, Simplified models of bolted joints under harmonic loading, Computers and Structures 84 (2005) 25–33.

[10] H. Ouyang, M.J. Oldfield, J.E. Mottershead, Experimental and theoretical studies of a bolted joint excited by a torsional dynamic load, International Journal of Mechanical Sciences 48 (2006) 1447–1455.

[11] D. Shetty, M.S. Allen, J.D. Schoneman, Application of the Bouc-Wen model to bolted joint dynamics, in: 38th International Modal Analysis Conference (IMAC XXXVIII), Houston, TX, February 2020.

[12] M.P. Mignolet, P. Song, X.Q. Wang, A stochastic Iwan-type model for joint behavior variability modeling, Journal of Sound and Vibration 349 (2015) 289–298. ISSN 0022-460X.

[13] B. Armstrong-Hélouvry, P. Dupont, C. Canudas de Wit, A survey of models, analysis tools and compensation methods for the control of machines with friction, Automatica 30 (1994) 1083–1138.

[14] M.R.W. Brake, A reduced Iwan model that includes pinning for bolted joint mechanics, Nonlinear Dynamics 87 (2) (2017) 1335–1349. ISSN 1573-269X.

[15] M. Eriten, A.A. Polycarpou, L.A. Bergman, Physics-based modeling for fretting behavior of nominally flat rough surfaces, International Journal of Solids and Structures 48 (10) (2011) 1436–1450. ISSN 0020-7683.

[16] N.N. Balaji, W. Chen, M.R.W. Brake, Traction-based multi-scale nonlinear dynamic modeling of bolted joints: Formulation, application, and trends in micro-scale interface evolution, Mechanical Systems and Signal Processing 139 (2020), 106615.

[17] D.M. Mulvihill, M.E. Kartal, D. Nowell, D.A. Hills, An elastic-plastic asperity interaction model for sliding friction, Tribology International 44 (2011) 1679–1694.

[18] K. Bode, G.P. Ostermeyer, A comprehensive approach for the simulation of heat and heat-induced phenomena in friction materials, Wear 311 (2014) 47–56.

[19] G.P. Ostermeyer, M. Müller, Dynamic interaction of friction and surface topography in brake systems, Tribology International 39 (2006) 370–380.

[20] M. Müller, G.P. Ostermeyer, Cellular automata method for macroscopic surface and friction dynamics in brake systems, Tribology International 40 (2007) 942–952.

[21] M. Müller, G.P. Ostermeyer, A cellular automation model to describe the three-dimensional friction and wear mechanism of brake systems, Wear 263 (2007) 1175–1188.

[22] M.R.W. Brake, C.W. Schwingshackl, P. Reuß, Observations of variability and repeatability in jointed structures, Mechanical Systems and Signal Processing 129 (2019) 282–307.

[23] M. Ruan, The variability of strains in bolts and the effect on preload in jointed structure, Masters thesis, Rice University, Houston, Texas, 2019.

[24] S.M. Sah, J.J. Thomsen, M. Brøns, A. Fidlin, D. Tcherniak, Estimating bolt tightness using transverse natural frequencies, Journal of Sound and Vibration 431 (2018) 137–149. ISSN 0022-460X.

[25] B.D. Yang, C.H. Menq, Modeling of friction contact and its application to the design of shroud contact, Journal of Engineering for Gas Turbines and Power 119 (4) (1997) 958–963.

[26] A. Visintin, Mathematical models of hysteresis, in: I. Mayergoyz, G. Bertotti (Eds.), The Science of Hysteresis, vol. 1, Elsevier Inc., 2005, pp. 1–123.

[27] M. Ismail, F. Ikhouane, J. Rodellar, The hysteresis Bouc-Wen model, a survey, Archives in Computational Methods in Engineering 16 (2009) 161–188.

[28] L. Pesaresi, J. Armand, C.W. Schwingshackl, L. Salles, C. Wong, An advanced underplatform damper modelling approach based on a microslip contact model, Journal of Sound and Vibration (2018). ISSN 0022-460X.

[29] Y. Song, C.J. Hartwigsen, D.M. McFarland, A.F. Vakakis, L.A. Bergman, Simulation of dynamics of beam structures with bolted joints using adjusted Iwan beam elements, Journal of Sound and Vibration 273 (2004) 249–276.

[30] A. Fantetti, L.R. Tamatam, M. Volvert, I. Lawal, L. Liu, L. Salles, M.R.W. Brake, C.W. Schwingshackl, D. Nowell, The impact of fretting wear on structural dynamics: Experiment and simulation, Tribology International 138 (2019) 111–124.

[31] L. Gaul, R. Nitsche, The role of friction in mechanical joints, ASME Applied Mechanics Reviews 54 (2001) 93–110.

[32] D.J. Segalman, M.J. Starr, Relationships Among Certain Joint Constitutive Models, Technical Report SAND2004-4321. Sandia National Laboratories, Albuquerque, NM, 2004.

[33] D.J. Segalman, An Initial Overview of Iwan Modeling for Mechanical Joints, Technical Report SAND2001-0811. Sandia National Laboratories, Albuquerque, NM, 2001.

[34] R. Bouc, Forced vibrations of mechanical systems with hysteresis, in: Proceedings of the Fourth Conference on Nonlinear Oscillations, Prague, 1967.

[35] Y.-K. Wen, Method for random vibration of hysteretic systems, ASCE Journal of the Engineering Mechanics Division 102 (1976) 249–263.

[36] S. Erlicher, N. Point, Thermodynamic admissibility of Bouc-Wen type hysteresis models, Comptes Rendus Mécanique 332 (2004) 51–57.

[37] K.C. Valanis, Fundamental consequences of a new intrinsic time measure. Plasticity as a limit of the endochronic theory, Technical Report G-224/DME-78-01, The University of Iowa, 1978.

[38] L. Gaul, J. Lenz, Nonlinear dynamics of structures assembled by bolted joints, Acta Mechanica 125 (1) (1997) 169–181. ISSN 1619-6937.

[39] J.R. Dormand, P.J. Prince, A family of embedded Runge-Kutta formulae, Journal of Computational and Applied Mathematics 6 (1980) 19–26.

[40] M. Peeters, R. Viguié, G. Sérandour, G. Kerschen, J.C. Golinval, Nonlinear normal modes, part II: Toward a practical computation using numerical continuation techniques, Mechanical Systems and Signal Processing 23 (2009) 195–216.

[41] M. Jin, W. Chen, M.R.W. Brake, H. Song, Identification of instantaneous frequency and damping from transient decay data, Journal of Vibration and Acoustics (2020) 1–36.

[42] Carl Edward Rasmussen, Christopher K.I. Williams, Gaussian processes for machine learning. Adaptive Computation and Machine Learning, MIT Press, Cambridge, Mass, 2006. ISBN 978-0-262-18253-9.

[43] R.M. Lacayo, M.S. Allen, Updating structural models containing nonlinear Iwan joints using quasi-static modal analysis, Mechanical Systems and Signal Processing 118 (2019) 133–157. ISSN 08883270.

[44] N.N. Balaji, T. Dreher, M. Krack, M.R.W. Brake, Reduced order modeling for the dynamics of jointed structures through hyper-reduced interface representation, Mechanical Systems and Signal Processing, Accepted.

[45] W.C. Hurty, Dynamic analysis of structural systems using component modes, AIAA Journal 3 (1960) 678–685.

[46] R.R. Craig, M.C.C. Bampton, Coupling of substructures for dynamic analyses, AIAA Journal 6 (7) (1968) 1313–1319.

[47] M.J.D. Powell, A Fortran subroutine for solving systems of nonlinear algebraic equations, Technical Report AERE-R-5947, Atomic Energy Research Establishment, Harwell, England (United Kingdom) (1968).

[48] A. Singh, M.S. Allen, R.J. Kuether, Substructure interface reduction with Iwan elements to capture nonlinearity, in: 38th International Modal Analysis Conference (IMAC XXXVIII), Houston, TX, February 2020.

[49] R.C. Flicek, M.R.W. Brake, D.A. Hills, Predicting a contact's sensitivity to initial conditions using metrics of frictional coupling, Tribology International 108 (2017) 95–110. ISSN 0301-679X.

[50] M. Krack, Nonlinear modal analysis of nonconservative systems: Extension of the periodic motion concept, Computers & Structures 154 (2015) 59–71. ISSN 00457949.

[51] N.N. Balaji, M.R.W. Brake, A quasi-static non-linear modal analysis procedure extending Rayleigh quotient stationarity for non-conservative dynamical systems, Computers and Structures 230 (2020) 106184. ISSN 0045-7949.

[52] J.J. Hollkamp, R.W. Gordon, Reduced-order models for nonlinear response prediction: Implicit condensation and expansion, Journal of Sound and Vibration 318 (4–5) (2008) 1139–1153.

[53] H. Festjens, G. Chevallier, J.-L. Dion, A numerical tool for the design of assembled structures under dynamic loads, International Journal of Mechanical Sciences 75 (2013) 170–177.

[54] M.S. Allen, R.M. Lacayo, M.R.W. Brake, Quasi-static modal analysis based on implicit condensation for structures with nonlinear joints, in: International Conference on Noise and Vibration Engineering, Leuven, Belgium, 2016.

[55] M. Krack, L. Salles, F. Thouverez, Vibration prediction of bladed disks coupled by friction joints, Archives of Computational Methods in Engineering 24 (3) (2017) 589–636. ISSN 1886-1784.

[56] D.J. Inman, Engineering Vibration. Pearson Education Inc, Upper Saddle River, New Jersey 07458, 4th edition, 2001. ISBN 0-13-287169-6.

[57] K. Deb, Multi-objective Optimization using Evolutionary Algorithms, vol. 16, John Wiley & Sons, 2001.

[58] I. Das, J.E. Dennis, Normal-boundary intersection: A new method for generating the Pareto surface in nonlinear multicriteria optimization problems, SIAM Journal on Optimization 8 (3) (1998) 631–657. ISSN 1052-6234. Publisher: Society for Industrial and Applied Mathematics.

[59] R.H. Byrd, J.C. Gilbert, J. Nocedal, A trust region method based on interior point techniques for nonlinear programming, Mathematical Programming 89 (1) (2000) 149–185. ISSN 1436-4646.

[60] R.A. Waltz, J.L. Morales, J. Nocedal, D. Orban, An interior algorithm for nonlinear optimization that combines line search and trust region steps, Mathematical Programming 107 (3) (2006) 391–408. ISSN 1436-4646.

[61] R.H. Byrd, M.E. Hribar, J. Nocedal, An interior point algorithm for large-scale nonlinear programming, SIAM Journal on Optimization 9 (4) (1999) 877–900. ISSN 1052-6234. Publisher: Society for Industrial and Applied Mathematics.

[62] S.A. Smith, M.R.W. Brake, C.W. Schwingshackl, On the characterization of nonlinearities in assembled structures, Journal of Vibration Acoustics 142 (5) (2020). ISSN 1048-9002.